HHS Public Access

Author manuscript

FASEB J. Author manuscript; available in PMC 2023 February 01.

Published in final edited form as:

FASEB J. 2022 February ; 36(2): e22157. doi:10.1096/fj.202101387R.

Mitigation of portal fibrosis and cholestatic liver disease in *ANKS6*-deficient livers by macrophage depletion

Merlin Airik[1,10], **Blake McCourt**[1,10], **Tugba Tastemel Ozturk**[2], **Amy B Huynh**[1], **Xiaoyi Zhang**[3], **Justin T Tometich**[4], **Rezan Topaloglu**[2], **Hasan Ozen**[5], **Diclehan Orhan**[6], **Kari Nejak-Bowen**[7], **Satdarshan P Monga**[7], **Timothy W Hand**[4], **Fatih Ozaltin**[2,8], **Rannar Airik**[1,9,*]

[1]Division of Nephrology, Department of Pediatrics, University of Pittsburgh, Pittsburgh, PA, USA

[2]Division of Pediatric Nephrology, Department of Pediatrics, Hacettepe University, Ankara, Turkey

[3]Division of Gastroenterology, Hepatology, and Nutrition, Department of Pediatrics, University of Pittsburgh, Pittsburgh, PA, USA

[4]R.K. Mellon Institute for Pediatric Research, Department of Pediatrics, Division of Infectious Disease, UPMC Children's Hospital of Pittsburgh, University of Pittsburgh, Pittsburgh, PA, 15224.

[5]Division of Gastroenterology, Department of Pediatrics, Hacettepe University, Ankara, Turkey

[6]Pediatric Pathology Unit, Department of Pediatrics, Hacettepe University, Ankara, Turkey

[7]Department of Pathology and Pittsburgh Liver Research Center, University of Pittsburgh and University of Pittsburgh Medical Center, Pittsburgh, Pennsylvania, USA

[8]Nephrogenetics Laboratory, Division of Pediatric Nephrology, Department of Pediatrics, Hacettepe University, Ankara, Turkey

[9]Department of Developmental Biology, University of Pittsburgh, Pittsburgh, Pennsylvania, USA

Abstract

Congenital hepatic fibrosis (CHF) is a developmental liver disease that is caused by mutations in genes that encode for ciliary proteins and is characterized by bile duct dysplasia and portal fibrosis. Recent work has demonstrated that mutations in *ANKS6* can cause CHF due to its role in bile duct development. Here, we report a novel *ANKS6* mutation, which was identified in an infant presenting with neonatal jaundice due to underlying biliary abnormalities and liver fibrosis. Molecular analysis revealed that *ANKS6* liver pathology is associated with the infiltration of inflammatory macrophages to the periportal fibrotic tissue and ductal epithelium. To further investigate the role of macrophages in CHF pathophysiology, we generated a novel liver-specific

[*]Corresponding Author: Name: Rannar Airik, PhD, Address: UPMC Children's Hospital of Pittsburgh, 4401 Penn Avenue, Pittsburgh, PA 15224, USA, airikr@pitt.edu, Tel.: +1 (412) 692-6229, Fax.: +1 (412) 692-7816.

[10]co-first authors

AUTHOR CONTRIBUTIONS

RA, MA, FA, XZ, TWH designed the experiments. RA, MA, BM, ABH performed genetic crosses, tissue sampling, and animal experiments. HO, TTO, RT, DO, FO, KNB and SM were involved in collecting and analyzing human tissue samples. TWH, XZ, JTT performed fluorescence-activated cell sorting experiments. RA, MA, BM, XZ, TWH, FO interpreted the data. RA, MA, XZ, TWH, FO wrote and reviewed the manuscript. RA supervised the project.

CONFLICT OF INTEREST STATEMENT

The authors have declared that no conflict of interest exists.

Anks6 knockout mouse model. The mutant mice develop biliary abnormalities and rapidly progressing periportal fibrosis reminiscent of human CHF. The development of portal fibrosis in *Anks6* KO mice coincided with the accumulation of inflammatory monocytes and macrophages in the mutant liver. Gene expression and flow cytometric analysis demonstrated the preponderance of M1- over M2-like macrophages at the onset of fibrosis. A critical role for macrophages in promoting peribiliary fibrosis was demonstrated by depleting the macrophages with clodronate liposomes which effectively reduced inflammatory gene expression and fibrosis, and ameliorated tissue histology and biliary function in *Anks6* KO livers. Together, this study demonstrates that macrophages play an important role in the initiation of liver fibrosis in *ANKS6*-deficient livers and their therapeutic elimination may provide an avenue to mitigate CHF in patients.

Keywords

ANKS6; nephronophthisis; congenital liver fibrosis; inflammation

INTRODUCTION

ANKS6 is a recently identified ciliary protein whose deficiency underlies a spectrum of developmental abnormalities in affected humans (OMIM 615382). Depending on the severity of the mutations, phenotypes can include kidney cysts, cardiovascular abnormalities, laterality defects and congenital hepatic fibrosis (CHF) [1–3]. While the precise function of ANKS6 remains to be determined, biochemical and functional studies of *Anks6* mutations have demonstrated that it is required for the formation and function of the cilium localized signaling compartment, known as Inversin (Inv)-compartment (IC) [4–7]. Indeed, mutations in genes which encode IC components – NPHP3, NPHP2/INV, NEK8, ANKS3 and ANKS6, result in phenotypically overlapping developmental abnormalities in affected humans [1, 8] and orthologous animal models [4, 8], underlining the critical role of each protein in the function of IC. One of the abnormalities shared by patients with mutations in these genes is congenital hepatic fibrosis (CHF), a developmental disorder of the liver that affects the portobiliary system and is associated with a spectrum of biliary abnormalities related to ductal plate remodeling defects [9]. The pathogenesis of CHF has been widely studied in mouse models deficient in the *PKHD1 ciliary IPT domain containing fibrocystin/polyductin* (*Pkhd1*) gene [10], which are orthologous to autosomal recessive polycystic kidney disease (ARPKD) in humans [11]. Using the $Pkhd1^{del4}$ mouse it was recently shown that portal fibrosis in CHF is driven by the accumulation of inflammatory macrophages around the bile ducts, and its progression could be mitigated by blocking macrophage accumulation [12]. Indeed, association between macrophage recruitment and portal fibrogenesis was also observed in the $Ift88^{Orpk}$ ciliopathy mouse model, in which abrogation of the expression of the *chemokine (C-C) motif ligand 2* (*Ccl2*) cytokine led to reduced infiltration of macrophages and fibrogenic disease in the liver [13]. Most recently it has been demonstrated that macrophages are critically involved in the progression of fibrogenesis in other forms of biliary fibrotic diseases, such as primary sclerosing cholangitis [14]. Whether macrophages play a role in the development of fibrosis in *ANKS6*-deficient livers is currently unknown.

The predominant type of macrophages in a healthy liver are Kupffer cells or resident macrophages that are derived from the yolk sac during embryonic development, and thereafter maintain their population in the liver through local proliferation [15]. In mouse, Kupffer cells are phenotypically characterized by the expression of $CD11b^{lo}F4/80^{hi}$ which is widely used to distinguish them from migratory macrophages, such as the bone marrow monocyte-derived macrophages that express $LyC6^{+}CD11b^{hi}F4/80^{lo}$ and are recruited to the liver upon injury [16–18]. Both resident and monocyte-derived macrophages play a critical role in the progression of portal fibrosis in chronic cholangiopathies due to their promotion of excessive inflammatory signaling through the secretion of tumor necrosis factor α, interleukin-1β and interleukin-6, among others [19, 20]. Importantly, macrophages also contribute to tissue repair and the resolution of fibrosis through the expression of various anti-inflammatory cytokines, such as interleukin-10 and arginase-1, and thus their depletion at the advanced stages of fibrosis can negatively affect tissue repair in the liver [21–23]. These observations underscore the exceptional phenotypic and functional plasticity of macrophages in response to cues from the local microenvironment and underlie the division of macrophages to classically activated or M1-like polarized and alternatively activated or M2-like polarized macrophages that are characterized by pro-inflammatory or anti-inflammatory cytokine expression profile, respectively [24].

Our current knowledge of the role of inflammatory macrophages in CHF pathogenesis is limited to a few forms of the disease – ARPKD due to *PKHD1* mutations [12] and primary sclerosing cholangitis [14]. Here, we hypothesized that inflammatory monocytes/macrophages play an important role in the pathogenesis of other genetic forms of CHF. To address this hypothesis, we performed an immunofluorescence analysis using macrophage-specific markers on a liver biopsy sample from a patient with congenital hepatic fibrosis caused by a homozygous mutation in the *ANKS6* gene. The analysis revealed an accumulation of both inflammatory M1-like, as well as profibrotic M2-like macrophages to the fibrotic tissue in the liver. The role of macrophages in the pathogenesis of portal fibrosis in *Anks6*-deficient livers was further studied by using a liver-specific *Anks6* knockout (KO) mouse model. We show that inactivation of *Anks6* expression in the liver results in bile duct morphogenesis defects and biliary epithelium hyperproliferation which are accompanied by rapidly progressive periportal fibrosis in postnatal livers. Functional studies revealed that portal fibrosis in *Anks6* KO mice is driven by the accumulation of inflammatory monocytes and macrophages in the peribiliary space in the mutant livers and can be reversed by therapeutic administration of clodronate liposomes which selectively kill phagocytosing macrophages. Collectively, these data show that *Anks6* KO mice are an orthologous model of human congenital hepatic fibrosis caused by mutations in the *ANKS6* gene and provide a rationale for using therapeutic inhibition of inflammatory macrophages to halt portal fibrogenesis in affected individuals.

MATERIAL AND METHODS

Mouse Breeding and Maintenance

Anks6loxP/loxP mice were maintained on a C57Bl6/J background and crossed with Albumin-Cre mouse strain (B6.Cg-Tg(Alb-cre)21Mgn/J, Stock #003574), which was

obtained from the Jackson Laboratory. PCR was used to genotype the mice. The experimental protocol was reviewed and approved by the Animal Care Committee of the University of Pittsburgh.

Treatment with Chlodronate-liposomes

Macrophage depletion in mice was performed using chlodronate-liposomes or PBS-liposomes (vehicle control) at a dose of 100 mg/kg through intraperitoneal injection (Encapsula NanoSciences). Liposomes were administered to the mice starting at 7 days of age on every 2nd day for the next 14 days, until the mice were 21 days old. The livers were collected, fixed and processed for downstream analysis.

Histological Analyses

Livers were fixed in 4% (w/v) paraformaldehyde in PBS at 4°C, after which they were dehydrated through a methanol series and embedded in paraffin. Sections were taken at 5 μm. Hematoxylin and eosin staining followed standard protocols. Sirius red staining was performed on deparaffinized sections according to manufacturer's instructions (Abcam, ab150681). Phenotyping in mouse embryos was performed blinded. More than 5 regions were selected at random and analyzed using Fiji [25].

Immunohistochemistry and antibodies

Paraffin Sections—Mouse livers were fixed in 4% (w/v) paraformaldehyde (PFA) in PBS at 4°C. Livers were then dehydrated through a methanol series and embedded in paraffin. Sections were taken at 5 μm. Samples were then deparaffinized and underwent antigen retrieval in sodium citrate buffer (pH6) in a pressure cooker for 18 minutes. Sections were blocked in 10% donkey serum/1% BSA/0.5% Triton X-100. Sections were incubated with primary antibodies overnight at 4°C. Sections were then incubated with secondary antibodies for 1 hour at room temperature.

Frozen sections—Mouse livers were fixed in 4% (w/v) paraformaldehyde (PFA) in PBS at 4°C for 10 minutes and then embedded in Tissue Freezing Medium (Triangle Biomedical Sciences, Inc.). Sections were taken at 8 μm using cryostat (Leica). Sections were blocked in 10% donkey serum/1% BSA/0.25% Tween-20 and permeabilized in 0.5% Triton X-100. Sections were incubated with primary antibodies overnight at 4°C. Sections were then incubated with secondary antibodies for 1 hour at room temperature. For immunofluorescence, sections were mounted with DAPI medium.

RNA Extraction and qRT–PCR

RNA was isolated from livers using Quick-RNA Miniprep Plus (Zymo Research). Reverse transcription was performed using iScript cDNA Synthesis Kit (Bio-Rad). Quantitative real-time PCR was carried out using iTaq Universal SYBR Green Supermix (Bio-Rad) and run on a CFX96 Touch™ Real-Time PCR Detection System (Bio-Rad). Data were normalized to *Gapdh* or *18S* as indicated. Real-time PCR primers are listed in Supplementary Table 2.

Antibodies

Primary antibodies are listed in Supplementary Table 1. Secondary antibodies were: donkey anti-mouse Alexa Fluor 488, donkey anti-mouse Alexa Fluor 594, donkey anti-rabbit Alexa Fluor 488, donkey anti-rabbit Alexa Fluor 594 (Molecular Probes), and goat anti-chicken Alexa Fluor 488 (Molecular Probes). Samples were mounted in ProlongGold (Molecular Probes) and images captured on a Leica TSC 5SP X confocal microscope (Leica Microsystems).

Flow cytometry and sorting

Intrahepatic leukocytes were isolated from 28 days old *Anks6* KO and control mouse livers for analysis by flow cytometry. After inferior vena cava saline flush, livers were isolated and minced for enzymatic digestion with 0.5 mg/mL DNase I and 0.02 mg/mL Liberase™ TL (Roche) in serum-free RPMI medium for 20 minutes at 37°C with agitation, prior to passage through 70μm filters. Leukocytes were separated by Ficoll gradient, followed by red blood cell lysis. Cells were stained with antibodies against mouse CD45.2, CD11b, Ly6C, MHC-II, and F4/80, with dead cell exclusion by LIVE/DEAD™ fixable viability stain (Invitrogen) on an LSRFortessa™ (BD Biosciences, San Jose, CA). Data were analyzed with FlowJo software (TreeStar Inc., Ashland, OR).

Blood serum analysis

Blood samples were collected using BD Microtainer® blood collection tubes (BD, Cat#365967) and stored at −80°C. Serum levels of total bilirubin were determined with a Bilirubin Assay Kit (Sigma-Aldrich, MAK126), and alanine aminotransferase levels with an Alanine Aminotransferase Activity Assay Kit (Sigma-Aldrich, MAK052).

Statistics

T-test was used to compare data between two groups. In treatment studies with clodronate statistical analysis was performed using two-way ANOVA and statistical significance was calculated using Tukey's multiple comparisons test. Pearson correlation coefficient was used to measure linear correlation between sets of data. In all analyses significance was determined at $p<0.05$ and represented by * to denote $p<0.05$, **$p<0.01$, ***$p<0.001$, ****$p<0.0001$. All experiments were carried out three times or more ($n\geq3$). Data were analyzed using Prism 9 software (GraphPad Software, San Diego, CA) and are given as the mean ± SEM.

Statement of Ethics

Human participants were ascertained and enrolled in the study after obtaining informed consent, in accordance with human subject research protocols approved by the ethical committee of Hacettepe University in Ankara (HEK 12/112–13). Liver samples from patients were obtained from the Pittsburgh Liver Research Center's Clinical Biospecimen Core under an approved IRB Study number 317222

Data availability

The authors declare that all other data supporting the findings of this study are available within the article and its Supplementary Information files.

RESULTS

Identification of a novel *ANKS6* splice-site mutation as a cause of congenital hepatic fibrosis in a neonatal child

A male newborn child of first-degree cousins was admitted to the hospital with jaundice when he was two days old (Figure 1A). The patient's physical examination was unremarkable, with laboratory evaluation notable for elevated liver enzymes and serum bilirubin, indicative of liver injury and cholestasis (see Supplementary Data for a detailed description of the clinical history). Abdominal ultrasonography was normal except for increased echogenicity of the kidneys. Using Sanger sequencing, we identified a novel homozygous acceptor splice-site variation in *ANKS6* (NM_173551.5): c.1618–2A>G (IVS8–2A>G) in the index patient (Figure 1B). The same variant was present in a heterozygous state in the parents and one of the 2 siblings, who are all healthy (Supplementary Figure 1A). The other healthy sibling showed wild type sequence in both alleles (Supplementary Figure 1B). To confirm that the splice-site variation has a functional consequence on *ANKS6* mRNA processing, we performed cDNA sequencing using peripheral blood derived mRNA, which demonstrated a skipping of *ANKS6* exon 9 (Figure 1C). At 6 months of age, the patient was diagnosed with chronic hepatitis, based on liver biopsy (IMHAI score 11, stage 5; HAI 12). By 2 years of age the patient had developed hepatosplenomegaly, and a second liver biopsy was performed, which showed bridging portal fibrosis and severe ductular reaction (Figure 1D). At this time the patient presented also with echogenic kidneys without cyst formation, periorbital edema, mild mitral and aortic valve regurgitation and mild aortic valve stenosis. Immunofluorescent analysis of the liver biopsy sample with antibodies against polyglutamylated tubulin, which labels the ciliary axoneme and ANKS6, revealed that the primary cilia are significantly shorter and lack ANKS6 expression in the patient bile duct epithelium compared to a healthy control sample (Figure 1E–G), demonstrating that the exon 9 skipping mutation affects bile duct cilia biogenesis and ANKS6 ciliary localization.

Together, these findings reveal a critical role for *ANKS6* in the development of multiple organ systems and are consistent with other reports showing that *ANKS6* splice-site mutations can cause congenital hepatic fibrosis and other liver abnormalities in humans [1, 3].

Macrophage recruitment is associated with portal fibrosis in *ANKS6*-deficient liver

Previous studies have shown that peribiliary fibrosis is associated with the accumulation of macrophages in multiple human fibrotic liver diseases, including CHF [12, 14, 26]. To investigate macrophage involvement in the pathogenesis of *ANKS6*-deficient liver disease, we performed an immunofluorescence staining of macrophages on the patient's liver biopsy at 2 years of age using antibodies against CD68 (a marker for resident and bone marrow-derived macrophages), CD163 (a marker of alternatively activated M2-like macrophages)

and HLA-DR (a marker of M1-like macrophages). We observed a significant accumulation of $CD68^+$, $CD163^+$ M2-like and $HLA\text{-}DR^+$ macrophages in the fibrotic tissue surrounding the portal bile ducts (Figure 2A–C). Quantification of the respective macrophage types in fibrotic vs adjacent parenchymal tissue revealed that the number of infiltrating macrophages was significantly higher in the fibrotic tissue compared to the non-fibrotic liver parenchyma. Importantly, the total number of $HLA\text{-}DR^+$ cells was higher than $CD163^+$ cells in the portal fibrotic area in the patient liver, suggesting a primarily proinflammatory environment at this stage of portal fibrosis. Moreover, tissue-infiltrating $CD68^+$ and HLA-DR+ macrophages were frequently observed to invade the bile duct lining epithelium, stained with cytokeratin 19 (CK19) or pan-cytokeratin proteins (panCK), respectively (Figure 2D–F).

Collectively, these data demonstrate that in addition to promoting portal inflammation and fibrosis, inflammatory monocytes/macrophages may cause bile duct destruction in individuals with *ANKS6*-deficiency, and thus play an important role in the pathophysiology of CHF.

Inactivation of *Anks6* in the developing liver causes biliary hyperplasia and cholestasis

To investigate the contribution of macrophages to the progression of congenital hepatic fibrosis caused by a loss of ANKS6 function, we generated a liver-specific *Anks6* knockout mouse line. Homozygous $Anks6^{flox}$ mice in which *Anks6* exon 2 is flanked by *loxP* sites were crossed with transgenic Albumin-Cre (Alb-Cre) mice, that express the Cre-recombinase in hepatoblast-derived cell lineages starting at embryonic day (E) 13.5 [27]. The resulting $Alb\text{-}Cre^{+};Anks6^{loxP/loxP}$ mice are hereafter referred to as *Anks6* KO or mutant mice, and the *Alb-Cre*-negative mice with $Alb\text{-}Cre^{-};Anks6^{loxP/loxP}$ or $Alb\text{-}Cre^{-};Anks6^{+/loxP}$ genotype are used as controls (ctrl) (Figure 3A). Genotyping was performed using allele-specific primers (Supplementary Figure 2A–D). Quantitative RT-PCR (qPCR) analysis of postnatal day (P) 7 *Anks6* KO mouse livers demonstrated a significant downregulation of *Anks6* mRNA expression, confirming a successful recombination of $Anks6^{loxP}$ alleles in the liver (Supplementary Figure 2E).

Anks6 KO mice were born at the expected Mendelian ratio with no overt abnormalities at birth. In the following weeks the mutant animals failed to thrive and appeared runted by P50 (Supplementary Figure 3A). While reduced body weight was observed in both sexes, it was more pronounced in male mice (Supplementary Figure 3B–E). Gross morphological analysis of *Anks6* KO livers at P21 and P50 revealed that the mutant livers were of similar size to the age-matched control livers but appeared invariably pale (Figure 3B). In addition, the mutant livers contained several necrotic spots that were discernible at a macroscopic view in 50 days old mice, consistent with development of cholestasis. Increase in liver to body weight ratio is observed in mouse models of cholestatic liver disease due to extensive portal fibrosis [28]. Indeed, both male and female *Anks6* KO animals demonstrated a significant liver to body weight ratio compared to control mice at 21 (Figure 3C) and 50 (Figure 3D) days of age. To assess liver histology in *Anks6* KO mice, we stained tissue sections from P7, P21, P50 and P100 days old animals with hematoxylin and eosin (Figure 3E–J, Supplementary Figure 4A). While liver parenchyma appeared unaffected in the mutant mice at these stages (Figure 3E,G,I), the portal histology demonstrated a collection of

tissue abnormalities that are characteristic of congenital hepatic fibrosis (CHF), including unremodeled and poorly differentiated bile ducts, as well as progressive peribiliary fibrosis (Figure 3F,H,J). At P50, the dysplastic biliary structures in *Anks6* KO livers were greatly expanded and enveloped by fibrotic tissue forming porto-portal bridging fibrosis (Figure 3I, J), contrasting the normal configuration of the biliary structures in control livers (Figure 3I, J). Consistent with the development of cholestasis, we frequently observed spotty lobular necrosis in the histological sections of *Anks6* KO livers at P50 (Figure 3I). In addition to liver abnormalities, *Anks6* KO mice develop splenomegaly by P28, consistent with portal hypertension secondary to CHF (Supplementary Figure 3F).

Together, these data demonstrate that *Anks6* KO mice recapitulate the histological and functional spectrum of liver phenotypes observed in humans with severe *ANKS6* mutations and validate the *Anks6* KO mouse as an orthologous model of human CHF.

Anks6 KO biliary hyperplasia is associated with increased cell cycle activity

To characterize the biliary morphology in *Anks6* KO mice in detail, we stained the mutant livers with antibodies against the cholangiocyte lineage marker, SRY-box transcription factor 9 (Sox9) and a mixture of cytokeratin proteins (panCK). In 1-week old control mice, the portal tract contained at least one well-defined bile duct that was positive for Sox9 and panCK expression, and a few unincorporated Sox9+ cells (Figure 4A). In contrast, the Sox9+ cells in *Anks6* KO livers remained in a single-layered ductal plate formation around the portal vein and did not yet form patent ductal structures (Figure 4A). By P21 and P50 the bile ducts in control animals were fully differentiated and localized in the proximity of portal veins, while the Sox9+ cholangiocytes in *Anks6* KO livers had expanded and formed numerous hyperplastic, disconnected, and segmentally dilated ductal structures, characteristic of ductal plate remodeling defects. To characterize the biliary expansion in *Anks6* KO livers we co-stained liver sections with the cell proliferation marker Ki67 and panCK and quantified the ratio of proliferating (Ki67+) cells to all cholangiocytes (panCK+) in the control and mutant livers at several postnatal ages. Cholangiocyte proliferation rates were unchanged between control and *Anks6* KO livers up to day 7 after birth (Figure 4B,C). However, as the mice aged cholangiocyte proliferation was significantly reduced in control livers, while it remained continuously elevated in *Anks6* KO livers through P21 and P50 (Figure 4B,C), demonstrating that biliary expansion in *Anks6* KO livers results from increased cholangiocyte proliferation.

To examine whether loss of *Anks6* affects bile duct maturation, we stained liver sections with antibodies against Ecadherin and Epcam. Both markers showed a normal expression pattern in the bile duct lining epithelium in *Anks6* KO livers compared to control livers (Supplementary Figure 5A), demonstrating that Anks6 function is not required for biliary differentiation.

Collectively, these data demonstrate that the primary biliary abnormalities in *Anks6* KO livers result from ductal plate remodeling defects, which lead to cholangiocyte hyperproliferation, biliary expansion and the formation of segmental bile duct dilations.

Bile duct expansion is accompanied by progressive portal fibrosis in *Anks6* KO livers

Our analysis above showed that *ANKS6* deficiency causes perinatal liver fibrosis (Figures 1 and 3, and [1, 7]). To characterize the onset and progression of portal fibrosis in detail, we stained *Anks6 KO* livers with Sirius red. We observed a steady increase in Sirius red-positive area in mutant livers as they aged compared to control livers (Figure 5A). Significant deposition of collagen occurred in *Anks6* KO livers between day 7 and 21, indicating a rapid postnatal progression of portal fibrosis. While the fibrogenesis was initially limited to individual portal tracts (P21 livers), it subsequently extended to form porto-portal bridges in the mutant livers (P50 and P100) (Figure 5A, Supplementary Figure 4B). Progressive development of portal fibrosis in *Anks6* KO animals was also demonstrated by the increased expansion of collagen 3-positive cells by IHC (Figure 5B), and increased expression of *collagen type 1a* (*Col1a*), *smooth muscle actin alpha 2* (*Acta2*) and *connective tissue growth factor* (*Ctgf*) mRNA (Figure 5C–E). Finally, we analyzed the expression of αSMA in *Anks6* KO livers, which showed a progressive age-dependent increase in *Anks6* KO mice compared to control mice (Supplementary Figure 6A,B), corroborating Sirius red staining analysis results.

Taken together, our data demonstrate that *Anks6* mutant mice develop congenital periportal liver fibrosis, replicating the human *ANKS6*-deficient liver phenotype.

Portal fibrosis is associated with pro-inflammatory signaling activity and an increase in macrophage recruitment

To investigate the role of inflammatory signaling and macrophage invasion in *ANKS6* liver fibrogenesis in detail, we analyzed the expression of various immune response-related genes in *Anks6* KO livers at pre- (P7), early (P21 and P50), and advanced (P100) stages of liver fibrosis, by immunofluorescence staining and qRT-PCR. Immunofluorescence staining of *Anks6* KO livers with the macrophage marker F4/80 revealed a significant accumulation of macrophages to the periportal areas at the onset of fibrogenesis in *Anks6* KO livers compared to control livers (Figure 6A). Accumulation of macrophages in *Anks6* KO livers was also reflected by the increase in *Emr1* (encoding F4/80) mRNA expression levels in P7, P21, P50 and P100 mutant livers (Figure 6B), and positively correlated with the increase in periportal fibrosis (Figure 6C).

Recruitment of macrophages to fibrotic lesions is driven by increased inflammatory signaling in the liver [13, 19, 20]. Indeed, the mRNA expression levels of the pro-inflammatory cytokines *macrophage chemoattractant cytokine 2* (*Ccl2*) and *tumor necrosis factor* (*Tnf*) were significantly increased in *Anks6* KO whole liver lysates already at P7 (Figure 6D), preceding overt liver fibrosis and macrophage invasion in these animals. The expression of *Ccl2* and *Tnf* peaked at P50 and became strongly reduced thereafter (Figure 6D). The expression profiles of two other inflammatory cytokines, *interleukin-1β (Il1β),* a pro-inflammatory cytokine, and *interleukin-6* (*Il6*), displayed a delayed expression in the liver. Both genes were expressed at basal levels in the mutant livers at P7, but became significantly upregulated at P21, after which *Il1β* expression was reduced to control levels, while *Il6* remained significantly increased in the mutant livers (Figure 6D). Interestingly the increase in pro-inflammatory cytokine gene expression was paralleled by a similar increase

in the expression of profibrotic genes, *integrin subunit beta 6* (*Itgb6*) and *transforming growth factor beta 1* (*Tgfb1*) in *Anks6* KO livers (Figure 6E,F). These data suggest that a complex interaction between pro-inflammatory and pro-fibrotic immune signaling pathways and cell types governs the onset of portal fibrogenesis and macrophage recruitment in *Anks6* KO livers. To determine the net effect of pro-inflammatory and pro-fibrotic cytokine expression on macrophage polarization in Anks6 KO livers, we examined the mRNA expression levels of *Nos2* (M1-like macrophage marker) and *Arginase 1* (*Arg1*) and *fibronectin 1* (*Fn1*) (both M2-like macrophage markers). *Nos2* expression was significantly increased at P21, after which it steadily declined, but remained significantly above the levels of control livers (Figure 6G). In contrast, the expression of *Arg1* and *Fn1* were consistently lower in *Anks6* KO livers compared with control livers at all ages examined (Figure 6H). Significantly, however, the relative ratio of M1/M2 macrophages, as determined by the ratio of *Nos2*/*Arg1* expression in *Anks6* KO livers was reduced as the mice aged (Figure 6I), supporting the notion that the macrophages acquire a more pro-fibrotic phenotype in advanced fibrosis.

Together, these data demonstrate that the onset of portal fibrogenesis in *Anks6* KO livers is associated with a strong pro-inflammatory signaling activity and accumulation of M1-like polarized macrophages. As the fibrosis progresses macrophage cytokine expression profile shifts to less inflammatory and more pro-fibrogenic expression in *Anks6* KO livers. Similar shift in macrophage polarization was observed in the fibrotic livers of aging *Pkhd1*^{del4} mice [12].

Inflammatory macrophages promote the progression of periportal fibrosis of *Anks6* KO mice

To characterize the cellular composition of the portal fibrosis in *Anks6* KO livers in detail, we performed flow cytometry analysis of 28 days old control and *Anks6* KO livers using monocyte and macrophage lineage markers (strategy shown in Figure 7A). These results showed that the total number of macrophages, defined as CD45^{+}CD11b^{+}F4/80^{+} was significantly increased in *Anks6* KO livers compared to control livers (Figure 7B). Similarly, the mutant livers contained significantly higher numbers of inflammatory monocytes (CD45^{+}CD11b^{+}F4/80^{-}Ly6C^{hi}MHCII^{-}) (Figure 7B). These data were confirmed by comparing the absolute number of CD11b^{+}F4/80^{+} macrophages from the whole liver and normalizing to average liver weight of 28 days old mice (Figure 7C). In contrast, the percentage of resident CD11b^{lo}F4/80^{hi} Kupffer cells was relatively low in the mutant livers in 28 days old *Anks6* KO mice (Figure 7D).

We next used IHC staining against CD206 to examine the presence of CD206^{+} alternatively activated (M2-like) pro-fibrotic macrophages in mutant liver at P7, P21, P50 and P100. Indeed, we observed a significant accumulation of CD206^{+} macrophages in the portal area of *Anks6* KO mice starting at P21 (Supplementary Figure 7A,B), and their numbers remained significantly increased through P50 and P100 (Supplementary Figure 7A,B). The peribiliary accumulation of CD206^{+} macrophages in *Anks6* KO livers is consistent with the role of CD206^{+} macrophages in promoting liver fibrosis [29].

Collectively, these data are in agreement with other reports showing that liver inflammation in CHF is accompanied by increased numbers of pro-inflammatory as well as pro-fibrotic monocytes and macrophages [12, 13, 30], and establish the *Anks6* KO mice as a relevant model to investigate the immune mechanisms in the pathogenesis of chronic hepatic fibrosis.

Clodronate-mediated depletion of macrophages reduces portal fibrosis and improves biliary function in *Anks6* KO livers

Elimination of macrophages by chemical or genetic means has been demonstrated to improve liver function and attenuate liver fibrosis across various liver injury models [12, 13, 20, 31, 32]. To examine whether macrophage ablation can be utilized to mitigate peribiliary fibrosis in *Anks6* KO livers we administered mice with clodronate liposomes (100 mg/kg) by intraperitoneal injection at every second day from day 7 to 21 after birth; the control cohort received PBS liposomes (Figure 8A). Clodronate liposomes significantly lowered the liver to body weight ratio in *Anks6* KO mice, but not in control mice after 2 weeks of treatment (Figure 8B), suggesting the effect is specific to mutant mice. In addition, spleen to bodyweight ratio was reduced in clodronate treated *Anks6* KO mice (Figure 8C), indicating a reduction in portal hypertension. Analysis of liver histology by Sirius red staining revealed a significant reduction in the fibrotic area in clodronate liposome-treated *Anks6* KO mice compared with mice that received PBS liposomes (Figure 8D). However, clodronate treatment had no effect on bile duct expansion in *Anks6* KO livers (Figure 8E). Consistent with Sirius red staining data, collagen 3 immunofluorescence staining was reduced in chlodronate treated *Anks6* KO livers (Figure 8F), as well as reduced expression of *Col1a*, *Acta2*, and *Ctgf* (Figure 8G), demonstrating that elimination of inflammatory macrophages effectively blocks fibrogenesis in the mutant livers. To examine the functional effect of clodronate treatment, we measured direct bilirubin levels in *Anks6* KO mice, which were significantly reduced compared to PBS liposome-treated mice (Figure 8H), demonstrating improved biliary function and reduced cholestasis after macrophage ablation. Interestingly, alanine aminotransferase (ALT) levels, slightly increased in *Anks6* KO mice at P21 compared to control mice, were unresponsive to clodronate treatment (Figure 8I), suggesting hepatocyte pathology in *Anks6* KO livers is not directly mediated by inflammatory macrophages.

Assessment of the expression of inflammatory cytokines in clodronate-treated *Anks6* KO livers by qPCR revealed a significant decrease in the mRNA levels of *Ccl2*, *Tnf*, *Il1β*, *Il6*, *Tgfb1*, *Itgb6* and *Emr1* consistent with reduced fibrosis and improved biliary function in these mice (Figure 9A,E,F,G). Clodronate liposomes also reduced the levels of both the canonical M1-like macrophage marker *Nos2* (Figure 9B) and alternatively activated M2-like macrophage markers *Arg1* and *Fn1* in the mutant livers (Figure 9C); however, the M1/M2 ratio based on *Nos2*/*Arg1* expression remained unchanged in clodronate vs. PBS liposome-treated mice (Figure 9D), indicating that non-selective depletion of inflammatory macrophages does not lead to a shift in the proportion of differentially polarized macrophages in the liver. This finding is consistent with the data by Locatelli et al., who showed no effect on M1 and M2 proportions in the liver after long term clodronate treatment [12].

Together, our results demonstrate that inflammatory macrophages are critical regulators of peribiliary fibrosis in *ANKS6*-deficient livers and their elimination at the onset of liver fibrosis is beneficial in preventing fibrogenesis and preserving biliary function.

DISCUSSION

Congenital hepatic fibrosis is a heterogeneous cholangiopathy that frequently manifests as part of cilia-related syndromic disorders, such as autosomal recessive polycystic kidney disease (OMIM #263200), Meckel-Gruber syndrome (OMIM #249000), Joubert syndrome (OMIM #213300), Bardet-Biedl syndrome (OMIM #209900), nephronophthisis (NPHP) (OMIM #256100) or oral-facial-digital syndrome (OMIM #311200), indicating that ciliary dysfunction which underpins the ductal plate remodeling abnormalities in these disorders can secondarily lead to progressive fibrogenesis in the portal tract [10, 33, 34]. Indeed, work by several groups, including ours, have demonstrated that defective bile duct morphogenesis gives rise to damaged and immature cholangiocytes, which secrete different profibrotic cytokines (Tgfb1) and growth factors (Ctgf) that promote cell proliferation and fibrogenesis in the surrounding tissue [7, 35, 36]. Immature cholangiocytes also secrete pro-inflammatory cytokines (Il1β, Il6, Tnf) and chemokines (Ccl2, Cxcl10), which leads to the accumulation of activated liver resident macrophages (Kupffer cells) and further propagation of inflammatory signaling in the portal tract and recruitment of inflammatory ($Ly6C^+$) bone marrow-derived monocytes to the sites of injury [19, 20]. Thus the general effect of portal inflammation is to trigger progressive fibrogenesis [12–14, 31]. The role of inflammatory macrophages in promoting the progression of portal fibrosis and mediating the repair of fibrotic lesions has been increasingly appreciated in recent years due to compelling pre-clinical and clinical evidence that blocking inflammatory signaling through genetic or pharmacological means results in amelioration of periportal fibrosis, which is the main determinant of development of portal hypertension and progression to liver failure [12–14, 21, 31, 32]. One of the limitations in extrapolating these experimental data to other syndromic forms of CHF is that the pathophysiology of CHF has been mostly studied using mouse models deficient in the *Pkhd1* gene [10], an orthologous model of human ARPKD.

Here we extend the ARPKD-based studies by reporting a novel *ANKS6* splice-site variant in a 2-days old child, who presented with neonatal jaundice due to underlying congenital hepatic fibrosis as part of a spectrum of other organ developmental defects, including chronic kidney disease and heart abnormalities. We showed that the variant leads to a structural change in the *ANSK6* mRNA by skipping exon 9. While we were not able to determine whether this mutation results in a loss or truncation of ANKS6 protein, our immunofluorescence analysis of the patient liver biopsy showed a complete absence of ANKS6 in the primary cilium of biliary epithelial cells, consistent with the notion that the mutation leads to a loss of ANKS6 ciliary function. Molecular analysis of the patient liver biopsy sample revealed that the liver pathology was associated with an accumulation of $CD68^+HLA\text{-}DR^+$ inflammatory macrophages in the periportal fibrotic lesions as well as their infiltration to the biliary epithelium. In addition, we observed a prominent presence of alternatively activated M2-like $CD163^+$ macrophages in the portal tract of the *ANKS6* patient liver biopsy sample. The role of CD68 or HLA-DR expressing macrophages in liver fibrosis has not been investigated in the context of CHF, previously. However, infiltration of

CD68$^+$ and HLA-DR$^+$ macrophages to the biliary epithelium has been observed in the liver biopsy samples from patients with primary biliary cholangitis (PBC) and primary sclerosing cholangitis [37–39], where their presence is associated with the destruction of the bile ducts [14, 37, 40]. In analogy to these liver diseases, we propose that the accumulation of CD68$^+$HLA-DR$^+$ macrophages in the peribiliary fibrotic tissue and infiltration to bile duct epithelium in the *ANKS6* patient liver biopsy indicates a strong inflammatory response to activated bile duct epithelial cells, whose destruction further perpetuates the inflammatory signaling, as observed in advanced stages of CHF [41]. Interestingly, we also observed an accumulation of anti-inflammatory CD163$^+$ macrophages in the inflammatory environment of the portal fibrosis in the *ANKS6* patient liver biopsy sample. Increased presence of CD163$^+$ macrophages has been reported in the fibrotic lesions of several inflammatory liver pathologies, such as non-alcoholic fatty liver disease [42], intrahepatic cholangiocarcinoma [43] and liver cirrhosis [44], where they are associated with advanced liver damage. Moreover, abundance of CD163+ macrophages in fibrosis has been shown to correlate with worse outcomes due to their anti-inflammatory and immune suppressive effects that inadvertently promote disease progression. It is highly likely that similar pathogenic mechanisms drive the liver pathology in CHF caused by *ANKS6* deficiency. Collectively, our phenotypic characterization of the macrophage populations in the *ANKS6* patient liver biopsy demonstrate that inflammatory macrophages play a critical role in CHF pathogenesis.

We expanded the observational human liver biopsy-based studies by functional assays in a liver-specific *Anks6* KO mouse model. Using the *Anks6* KO mouse, we show that 1) *Anks6* KO livers recapitulate the histological and functional abnormalities of human *ANKS6* deficiency; 2) progression of portal fibrosis is associated with the accumulation of inflammatory macrophages; and 3) depletion of macrophages through the administration of clodronate liposomes mitigates loss of biliary function and blocks the progression of periportal fibrosis, but not bile duct expansion.

In our mouse model, the primary defect in early postnatal *Anks6* KO livers was restricted to the bile duct epithelium. While the specific defect(s) underlying the epithelial pathology was not examined in this study, our analysis demonstrated a marked cholangiocyte hyperproliferation in mutant postnatal livers which led to biliary expansion. In fact, biliary hyperplasia and bile duct expansion are hallmark features of CHF in humans and observed in biopsies from patients with mutations in *PKHD1* [45], *DZIP1L* [46], or *NPHP3* [8]. Coincident with the biliary expansion between day 7 and 21, we observed a rapid progression of periportal fibrogenesis in *Anks6* KO mouse livers, suggesting that a failure to establish functional bile ducts due to the loss of ANKS6 biliary function, secondarily activates the fibrogenic program in the periportal mesenchyme. Indeed, it is well documented that proliferating biliary epithelium is a major source of Ctgf, Tgfb1 and Itgb6, which promote portal fibrogenesis [36, 47, 48]. Importantly, all three genes were upregulated in 21 days old *Anks6* KO livers compared to control mice, underlying the increase in peribiliary collagen deposition (Sirius red staining) and activation of myofibroblasts (αSMA+ cells) in the mutant livers.

Careful expression analyses of inflammatory cytokines, chemokines and macrophage markers from 7 to 100 days old *Anks6* KO livers enabled us to reconstruct the dynamics

of inflammatory and fibrogenic gene expression as the portal fibrosis progressed. The central finding from these analyses is that progressive portal fibrosis in *Anks6* KO mice is associated with activation of inflammatory signaling and macrophage recruitment. The kinetics of cytokine and chemokine expression in *Anks6* KO livers suggest that the expression of inflammatory cytokines was increased before a significant increase in portal fibrosis (Sirius red), αSMA or Collagen 3 expression was observed. In agreement with other models of CHF [12, 13, 31], the inflammatory signaling in *Anks6* mutant livers was characterized by an increase in *Ccl2* expression already at postnatal day 7. Concordantly, FACS analysis of 28 days old livers showed an increase of $Ly6C^{+}$ inflammatory monocytes in the mutant mice, suggestive of recruitment of migratory monocytes and macrophages to the liver [49]. Indeed, comparison of the proportions of $CD11b^{lo}F4/80^{hi}$ resident macrophages in the early stage of fibrogenesis (28 days old mice) demonstrated a relative reduction in the ratio of resident macrophages in control vs *Anks6* KO livers, indicative of a predominant role of migratory monocytes/macrophages in the promotion of fibrosis in *Anks6* KO livers. Characteristic of a strong inflammatory milieu, whole liver qPCR analysis revealed a significant increase in the expression of *Nos2* and other pro-inflammatory cytokines (*Tnf*, *Il1b*, *Il6*) during the early stages of fibrogenesis in *Anks6* KO livers, suggesting that pro-inflammatory and anti-fibrotic immune signaling pathways dominate at the whole organ level during the onset of portal fibrosis in *Anks6* KO livers. On the other hand, we did observe local enrichment of pro-fibrotic $CD206^{+}$ macrophages in the peribiliary space in 21-days old *Anks6* KO mice by IHC, suggesting that some pro-fibrotic cues are expressed by the biliary epithelium in the mutant livers. Indeed, this finding corroborates the macrophage phenotyping data in *ANK6* patient liver biopsy and is consistent with the known distribution of macrophage phenotypes during liver fibrosis [30]. In addition, local accumulation of the pro-fibrotic $CD206^{+}$ macrophages around bile ducts is consistent with the observed increase in portal fibrosis in *Anks6* KO livers starting at 21 days of age.

We also provide evidence that accumulation of inflammatory macrophages is an important driver of the portal fibrogenesis in *Anks6* KO livers by demonstrating depletion of macrophages with liposomal clodronate before the onset of overt liver fibrogenesis effectively reduced portal fibrosis, preserving the portal histology, and improved biliary function in *Anks6* KO livers. Indeed, our demonstration that periportal fibrogenesis in *ANKS6*-deficient livers is mechanistically linked to the accumulation of inflammatory monocytes/macrophages in humans and an orthologous *Anks6* KO mouse model provides a compelling support to the idea that congenital hepatic fibrosis is driven by the activation of pro-inflammatory signaling in the periportal space by activated bile duct epithelial cells and extends the findings of the *Pkhd1* mouse model [12]. There are also some noticeable differences in the liver pathophysiology between $Pkhd1^{del4}$ and *Anks6* KO mouse model. Importantly, the pathogenesis of periportal fibrosis is significantly slower in $Pkhd1^{del4}$ mice (onset around 3 months) [12], compared to a very rapid development of portal fibrosis in *Anks6* KO mice (21 days). Similarly, expression of the pro-inflammatory cytokines occurred much earlier in *Anks6* KO livers. Furthermore, while mutations in *Pkhd1* cause a cystic liver disease, biliary cysts were never observed in *Anks6* KO livers.

A central finding in this study is that inflammatory monocytes/macrophages are important components of the CHF pathogenesis, regardless of the underlying genetic mutations. Further investigations are thus warranted to investigate which monocyte/macrophage populations should be targeted to mitigate the inflammatory reaction in CHF and whether the target cells differ based on the stage of the disease, i.e. M1-like vs M2-like macrophages.

Supplementary Material

Refer to Web version on PubMed Central for supplementary material.

ACKNOWLEDGEMENTS

This research was supported by grants from the National Institutes of Health to R.A. (DK099434, DK115403, P30DK079307). The human disease samples were provided in part by the Pittsburgh Liver Research Center funded by P30DK120531 (SPM).

NONSTANDARD ABBREVIATIONS

Acta2	smooth muscle actin alpha 2
ADPKD	autosomal dominant polycystic kidney disease
Alb	albumin
ALT	alanine aminotransferase
ANKS3	ankyrin repeat and sterile alpha motif domain containing 3
ANKS6	ankyrin repeat and sterile alpha motif domain containing 6
Arg	arginase-1
ARPKD	autosomal recessive polycystic kidney disease
αSMA	alpha smooth muscle actin
BSA	bovine serum albumin
CCL2	chemokine (C-C) motif ligand 2
CCR2	C-C chemokine receptor 2
CD11b	cluster of differentiation molecule 11B
CD163	cluster of differentiation 163
CD206	cluster of differentiation 206
CD45	cluster of differentiation 45
CD68	cluster of differentiation 68
CHF	congenital hepatic fibrosis
CK	cytokeratin

Col1a	collagen type 1a
Cre	Cre recombinase
Ctgf	connective tissue growth factor
Cxcl10	C-X-C motif chemokine ligand 10
DZIP1L	DAZ interacting zinc finger protein 1 like
E	embryonic day
Emr1	EGF-like module-containing mucin-like hormone receptor-like 1
Epcam	Epithelial cell adhesion molecule
F4/80	protein encoded by Emr1 gene
Flox	locus of X-over P1
Fn1	fibronectin
HAI	histology activity index
HLA-DR	Human Leukocyte Antigen – DR isotype
IC	Inversin compartment
Il10	interleukin-10
Il1b	interleukin-1β
Il6	interleukin-6
IMHAI	Ishak modified histology activity index
Itgb6	integrin subunit beta 6
IVS	Intervening sequence
kg	kilogram
KO	knockout
loxP	locus of X-over P1
LyC6	lymphocyte antigen 6 complex, locus C1
M1	M1 macrophage
M2	M2 macrophage
mg	milligram
MHCII	major histocompatibility complex class II
mRNA	messenger ribonucleic acid

NEK8	NIMA related kinase 8
Nos2	nitric oxide synthase 2
NPHP2/INV	Nephrocystin 2/Inversin
NPHP3	Nephrocystin 3
OMIM	Online Mendelian Inheritance in Man
P	postnatal day
panCK	pan cytokeratin proteins
PBC	primary biliary cholangitis
PCK	polycystic kidney
PCR	polymerase chain reaction
PFA	paraformaldehyde
PKHD1	ciliary IPT domain containing fibrocystin/polyductin gene
qRT–PCR	quantitative reverse transcription polymerase chain reaction
SEM	standard error of mean
Sox9	SRY-box transcription factor 9
Tgfb1	transforming growth factor beta 1
TNF	tumor necrosis factor α
v	volume
w	weight
μm	micrometer

REFERENCES

[1]. Hoff S, Halbritter J, Epting D, Frank V, Nguyen TM, van Reeuwijk J, et al. ANKS6 is a central component of a nephronophthisis module linking NEK8 to INVS and NPHP3. Nat Genet 2013;45:951–956. [PubMed: 23793029]

[2]. Taskiran EZ, Korkmaz E, Gucer S, Kosukcu C, Kaymaz F, Koyunlar C, et al. Mutations in ANKS6 cause a nephronophthisis-like phenotype with ESRD. J Am Soc Nephrol 2014;25:1653–1661. [PubMed: 24610927]

[3]. Kulkarni S, Abro B, Duque Lasio ML, Stoll J, Grange DK, He M. Clinical and Pathological Features of a Newborn With Compound Heterozygous ANKS6 Variants. Pediatr Dev Pathol 2020;23:235–239. [PubMed: 31635528]

[4]. Czarnecki PG, Gabriel GC, Manning DK, Sergeev M, Lemke K, Klena NT, et al. ANKS6 is the critical activator of NEK8 kinase in embryonic situs determination and organ patterning. Nat Commun 2015;6:6023. [PubMed: 25599650]

[5]. Nakajima Y, Kiyonari H, Mukumoto Y, Yokoyama T. The Inv compartment of renal cilia is an intraciliary signal-activating center to phosphorylate ANKS6. Kidney Int 2018;93:1108–1117. [PubMed: 29395339]

[6]. Bennett HW, Gustavsson AK, Bayas CA, Petrov PN, Mooney N, Moerner WE, et al. Novel fibrillar structure in the inversin compartment of primary cilia revealed by 3D single-molecule superresolution microscopy. Mol Biol Cell 2020;31:619–639. [PubMed: 31895004]

[7]. Airik M, Schuler M, McCourt B, Weiss AC, Herdman N, Ludtke TH, et al. Loss of Anks6 leads to YAP deficiency and liver abnormalities. Hum Mol Genet 2020;29:3064–3080. [PubMed: 32886109]

[8]. Bergmann C, Fliegauf M, Bruchle NO, Frank V, Olbrich H, Kirschner J, et al. Loss of nephrocystin-3 function can cause embryonic lethality, Meckel-Gruber-like syndrome, situs inversus, and renal-hepatic-pancreatic dysplasia. Am J Hum Genet 2008;82:959–970. [PubMed: 18371931]

[9]. Liver Gunay-Aygun M. and kidney disease in ciliopathies. Am J Med Genet C Semin Med Genet 2009;151C:296–306. [PubMed: 19876928]

[10]. Guay-Woodford LM. Autosomal recessive polycystic kidney disease: the prototype of the hepato-renal fibrocystic diseases. J Pediatr Genet 2014;3:89–101. [PubMed: 25632369]

[11]. Ward CJ, Hogan MC, Rossetti S, Walker D, Sneddon T, Wang X, et al. The gene mutated in autosomal recessive polycystic kidney disease encodes a large, receptor-like protein. Nat Genet 2002;30:259–269. [PubMed: 11919560]

[12]. Locatelli L, Cadamuro M, Spirli C, Fiorotto R, Lecchi S, Morell CM, et al. Macrophage recruitment by fibrocystin-defective biliary epithelial cells promotes portal fibrosis in congenital hepatic fibrosis. Hepatology 2016;63:965–982. [PubMed: 26645994]

[13]. Zimmerman KA, Song CJ, Gonzalez-Mize N, Li Z, Yoder BK. Primary cilia disruption differentially affects the infiltrating and resident macrophage compartment in the liver. Am J Physiol Gastrointest Liver Physiol 2018;314:G677–G689. [PubMed: 29543508]

[14]. Guicciardi ME, Trussoni CE, Krishnan A, Bronk SF, Lorenzo Pisarello MJ, O'Hara SP, et al. Macrophages contribute to the pathogenesis of sclerosing cholangitis in mice. J Hepatol 2018;69:676–686. [PubMed: 29802947]

[15]. Gomez Perdiguero E, Klapproth K, Schulz C, Busch K, Azzoni E, Crozet L, et al. Tissue-resident macrophages originate from yolk-sac-derived erythro-myeloid progenitors. Nature 2015;518:547–551. [PubMed: 25470051]

[16]. Dal-Secco D, Wang J, Zeng Z, Kolaczkowska E, Wong CH, Petri B, et al. A dynamic spectrum of monocytes arising from the in situ reprogramming of CCR2+ monocytes at a site of sterile injury. J Exp Med 2015;212:447–456. [PubMed: 25800956]

[17]. Katsumi T, Guicciardi ME, Azad A, Bronk SF, Krishnan A, Gores GJ. Activated cholangiocytes release macrophage-polarizing extracellular vesicles bearing the DAMP S100A11. Am J Physiol Cell Physiol 2019;317:C788–C799. [PubMed: 31365294]

[18]. Guillot A, Guerri L, Feng D, Kim SJ, Ahmed YA, Paloczi J, et al. Bile acid-activated macrophages promote biliary epithelial cell proliferation through integrin alphavbeta6 upregulation following liver injury. J Clin Invest 2021;131.

[19]. Best J, Verhulst S, Syn WK, Lagaisse K, van Hul N, Heindryckx F, et al. Macrophage Depletion Attenuates Extracellular Matrix Deposition and Ductular Reaction in a Mouse Model of Chronic Cholangiopathies. PLoS One 2016;11:e0162286. [PubMed: 27618307]

[20]. Jemail L, Miyao M, Kotani H, Kawai C, Minami H, Abiru H, et al. Pivotal roles of Kupffer cells in the progression and regression of DDC-induced chronic cholangiopathy. Sci Rep 2018;8:6415. [PubMed: 29686325]

[21]. Duffield JS, Forbes SJ, Constandinou CM, Clay S, Partolina M, Vuthoori S, et al. Selective depletion of macrophages reveals distinct, opposing roles during liver injury and repair. J Clin Invest 2005;115:56–65. [PubMed: 15630444]

[22]. Mitchell C, Couton D, Couty JP, Anson M, Crain AM, Bizet V, et al. Dual role of CCR2 in the constitution and the resolution of liver fibrosis in mice. Am J Pathol 2009;174:1766–1775. [PubMed: 19359521]

[23]. Wynn TA, Ramalingam TR. Mechanisms of fibrosis: therapeutic translation for fibrotic disease. Nat Med 2012;18:1028–1040. [PubMed: 22772564]

[24]. Murray PJ. Macrophage Polarization. Annu Rev Physiol 2017;79:541–566. [PubMed: 27813830]

[25]. Schindelin J, Arganda-Carreras I, Frise E, Kaynig V, Longair M, Pietzsch T, et al. Fiji: an open-source platform for biological-image analysis. Nat Methods 2012;9:676–682. [PubMed: 22743772]

[26]. Mousa HS, Carbone M, Malinverno F, Ronca V, Gershwin ME, Invernizzi P. Novel therapeutics for primary biliary cholangitis: Toward a disease-stage-based approach. Autoimmun Rev 2016;15:870–876. [PubMed: 27393766]

[27]. Postic C, Shiota M, Niswender KD, Jetton TL, Chen Y, Moates JM, et al. Dual roles for glucokinase in glucose homeostasis as determined by liver and pancreatic beta cell-specific gene knock-outs using Cre recombinase. J Biol Chem 1999;274:305–315. [PubMed: 9867845]

[28]. Zhang N, Bai H, David KK, Dong J, Zheng Y, Cai J, et al. The Merlin/NF2 tumor suppressor functions through the YAP oncoprotein to regulate tissue homeostasis in mammals. Dev Cell 2010;19:27–38. [PubMed: 20643348]

[29]. Tan-Garcia A, Lai F, Sheng Yeong JP, Irac SE, Ng PY, Msallam R, et al. Liver fibrosis and CD206(+) macrophage accumulation are suppressed by anti-GM-CSF therapy. JHEP Rep 2020;2:100062. [PubMed: 32039403]

[30]. Beljaars L, Schippers M, Reker-Smit C, Martinez FO, Helming L, Poelstra K, et al. Hepatic Localization of Macrophage Phenotypes during Fibrogenesis and Resolution of Fibrosis in Mice and Humans. Front Immunol 2014;5:430. [PubMed: 25250030]

[31]. Kaffe E, Fiorotto R, Pellegrino F, Mariotti V, Amenduni M, Cadamuro M, et al. beta-Catenin and interleukin-1beta-dependent chemokine (C-X-C motif) ligand 10 production drives progression of disease in a mouse model of congenital hepatic fibrosis. Hepatology 2018;67:1903–1919. [PubMed: 29140564]

[32]. Baeck C, Wei X, Bartneck M, Fech V, Heymann F, Gassler N, et al. Pharmacological inhibition of the chemokine C-C motif chemokine ligand 2 (monocyte chemoattractant protein 1) accelerates liver fibrosis regression by suppressing Ly-6C(+) macrophage infiltration in mice. Hepatology 2014;59:1060–1072. [PubMed: 24481979]

[33]. Desmet VJ. Ludwig symposium on biliary disorders--part I. Pathogenesis of ductal plate abnormalities. Mayo Clin Proc 1998;73:80–89. [PubMed: 9443684]

[34]. Cadamuro M, Girardi N, Gores GJ, Strazzabosco M, Fabris L. The Emerging Role of Macrophages in Chronic Cholangiopathies Featuring Biliary Fibrosis: An Attractive Therapeutic Target for Orphan Diseases. Front Med (Lausanne) 2020;7:115. [PubMed: 32373615]

[35]. Moser M, Matthiesen S, Kirfel J, Schorle H, Bergmann C, Senderek J, et al. A mouse model for cystic biliary dysgenesis in autosomal recessive polycystic kidney disease (ARPKD). Hepatology 2005;41:1113–1121. [PubMed: 15830394]

[36]. Sedlaczek N, Jia JD, Bauer M, Herbst H, Ruehl M, Hahn EG, et al. Proliferating bile duct epithelial cells are a major source of connective tissue growth factor in rat biliary fibrosis. Am J Pathol 2001;158:1239–1244. [PubMed: 11290541]

[37]. Wu CT, Eiserich JP, Ansari AA, Coppel RL, Balasubramanian S, Bowlus CL, et al. Myeloperoxidase-positive inflammatory cells participate in bile duct damage in primary biliary cirrhosis through nitric oxide-mediated reactions. Hepatology 2003;38:1018–1025. [PubMed: 14512889]

[38]. Spengler U, Pape GR, Hoffmann RM, Johnson JP, Eisenburg J, Paumgartner G, et al. Differential expression of MHC class II subregion products on bile duct epithelial cells and hepatocytes in patients with primary biliary cirrhosis. Hepatology 1988;8:459–462. [PubMed: 3371866]

[39]. Chapman RW, Kelly PM, Heryet A, Jewell DP, Fleming KA. Expression of HLA-DR antigens on bile duct epithelium in primary sclerosing cholangitis. Gut 1988;29:422–427. [PubMed: 3286382]

[40]. Sasaki M, Kakuda Y, Miyakoshi M, Sato Y, Nakanuma Y. Infiltration of inflammatory cells expressing mitochondrial proteins around bile ducts and in biliary epithelial layer may be involved in the pathogenesis in primary biliary cirrhosis. J Clin Pathol 2014;67:470–476. [PubMed: 24407434]

[41]. Desmet VJ. Congenital diseases of intrahepatic bile ducts: variations on the theme “ductal plate malformation”. Hepatology 1992;16:1069–1083. [PubMed: 1398487]

[42]. De Vito R, Alisi A, Masotti A, Ceccarelli S, Panera N, Citti A, et al. Markers of activated inflammatory cells correlate with severity of liver damage in children with nonalcoholic fatty liver disease. Int J Mol Med 2012;30:49–56. [PubMed: 22505182]

[43]. Hasita H, Komohara Y, Okabe H, Masuda T, Ohnishi K, Lei XF, et al. Significance of alternatively activated macrophages in patients with intrahepatic cholangiocarcinoma. Cancer Sci 2010;101:1913–1919. [PubMed: 20545696]

[44]. Xi S, Zheng X, Li X, Jiang Y, Wu Y, Gong J, et al. Activated Hepatic Stellate Cells Induce Infiltration and Formation of CD163(+) Macrophages via CCL2/CCR2 Pathway. Front Med (Lausanne) 2021;8:627927. [PubMed: 33614685]

[45]. Sanzen T, Harada K, Yasoshima M, Kawamura Y, Ishibashi M, Nakanuma Y. Polycystic kidney rat is a novel animal model of Caroli’s disease associated with congenital hepatic fibrosis. Am J Pathol 2001;158:1605–1612. [PubMed: 11337358]

[46]. Lu H, Galeano MCR, Ott E, Kaeslin G, Kausalya PJ, Kramer C, et al. Mutations in DZIP1L, which encodes a ciliary-transition-zone protein, cause autosomal recessive polycystic kidney disease. Nat Genet 2017;49:1025–1034. [PubMed: 28530676]

[47]. Popov Y, Patsenker E, Stickel F, Zaks J, Bhaskar KR, Niedobitek G, et al. Integrin alphavbeta6 is a marker of the progression of biliary and portal liver fibrosis and a novel target for antifibrotic therapies. J Hepatol 2008;48:453–464. [PubMed: 18221819]

[48]. Patsenker E, Popov Y, Stickel F, Jonczyk A, Goodman SL, Schuppan D. Inhibition of integrin alphavbeta6 on cholangiocytes blocks transforming growth factor-beta activation and retards biliary fibrosis progression. Gastroenterology 2008;135:660–670. [PubMed: 18538673]

[49]. Geissmann F, Manz MG, Jung S, Sieweke MH, Merad M, Ley K. Development of monocytes, macrophages, and dendritic cells. Science 2010;327:656–661. [PubMed: 20133564]

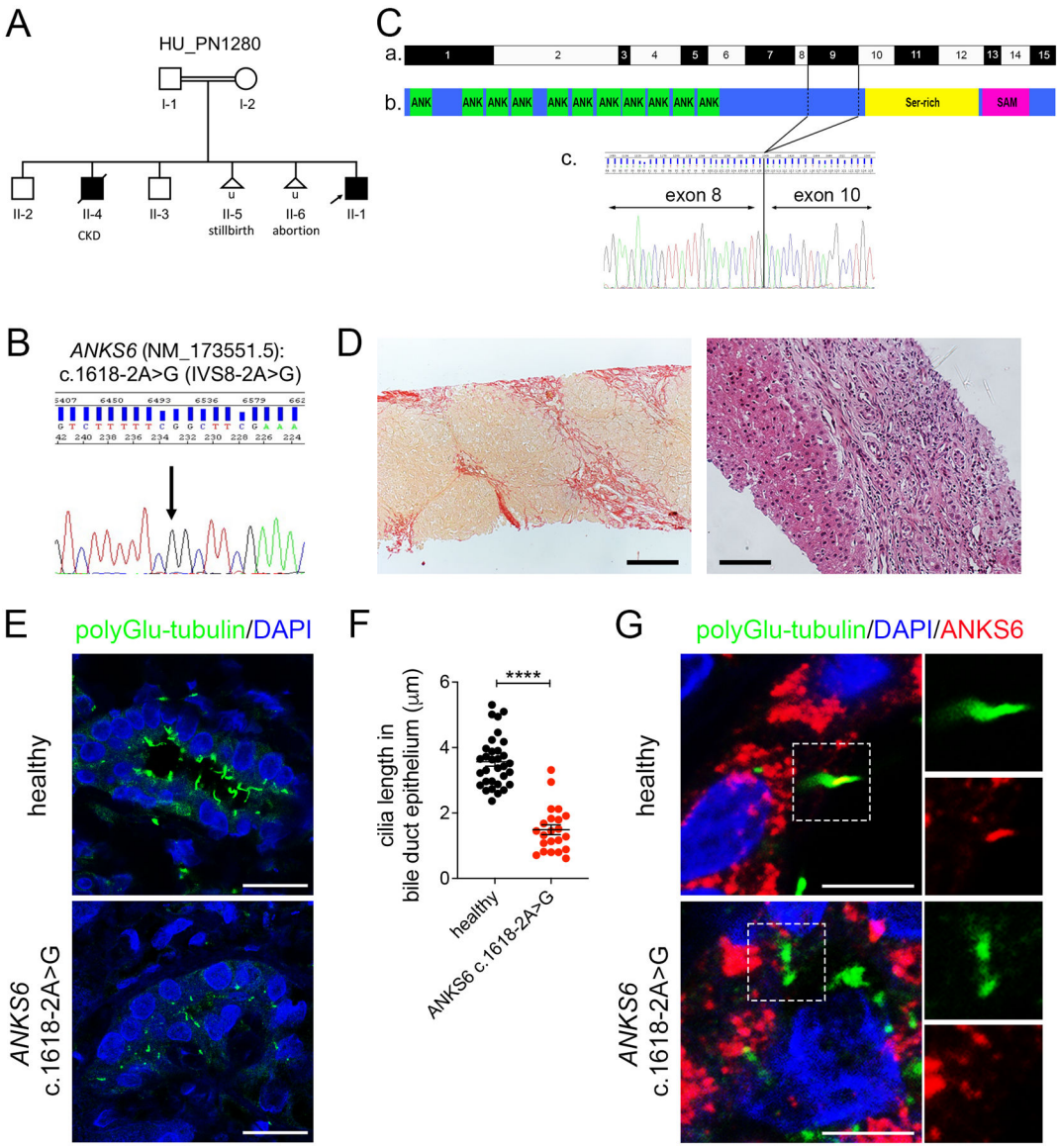

Figure 1. Identification of a novel homozygous *ANKS6* mutation in a patient with hepatorenal fibrocystic disease.

(**A**) Pedigree of a consanguineous Turkish family (HU_PN1280) with chronic hepatitis, echogenic kidneys and mild aortic stenosis. Index patient is indicated with an arrow.

(**B**) Homozygous variation in *ANKS6* (NM_173551.5) c.1618–2A>G (IVS8–2A>G) was identified in the index patient HU_PN1280-II1, affecting the consensus acceptor splice site in intron 8 that segregates with the disease. CDK, chronic kidney disease; u, unidentified gender.

(**C**) The schematic depicts the exon structure of human ANKS6 (**a**) and its effect on cDNA structure by skipping exon 9 (**b**). cDNA sequencing of patient lymphocytes confirmed that the acceptor splice site variation results in skipping of exon 9 in *ANKS6* mRNA (**c**). ANK, ankyrin domain; Ser-rich, serine-rich region; SAM, sterile alpha motive.

(**D**) Needle core liver biopsy from the patient shows portal to portal bridging fibrosis (Sirius red staining), and ductal plate abnormalities (hematoxylin and eosin staining). Scale bars, 200 μm and 100 μm, respectively.

(**E**) Immunofluorescent staining against polyglutamylated tubulin (green) marks the primary cilia in the bile duct lining epithelial cells in the healthy and *ANKS6*-deficient individual. Scale bars 20 μm.

(**F**) Quantification of the primary cilia length in the bile duct lining epithelium reveals that the biliary cilia are significantly shorter in the *ANKS6* patient compared to a healthy control (control cilia length 3.6 μm ± 0.4 μm n=32 cells vs. *ANKS6* 1.5 μm ± 0.1 μm n=22 cells, ****p<0.0001). Results analyzed by t-test

(**G**) Co-staining of liver biopsy samples against polyglutamylated tubulin (green) and ANKS6 (red) demonstrates the normal localization of ANKS6 in the proximal part of the primary cilia in a healthy individual, whereas no ANKS6 expression is observed in the biliary cilia in the individual with *ANKS6* c.1618–2A>G mutation. The source of the cytoplasmic red signal (ANKS6 channel) in the bile duct epithelial cells in the healthy and diseased livers is not known but is likely artefactual. Scale bars 5 μm.

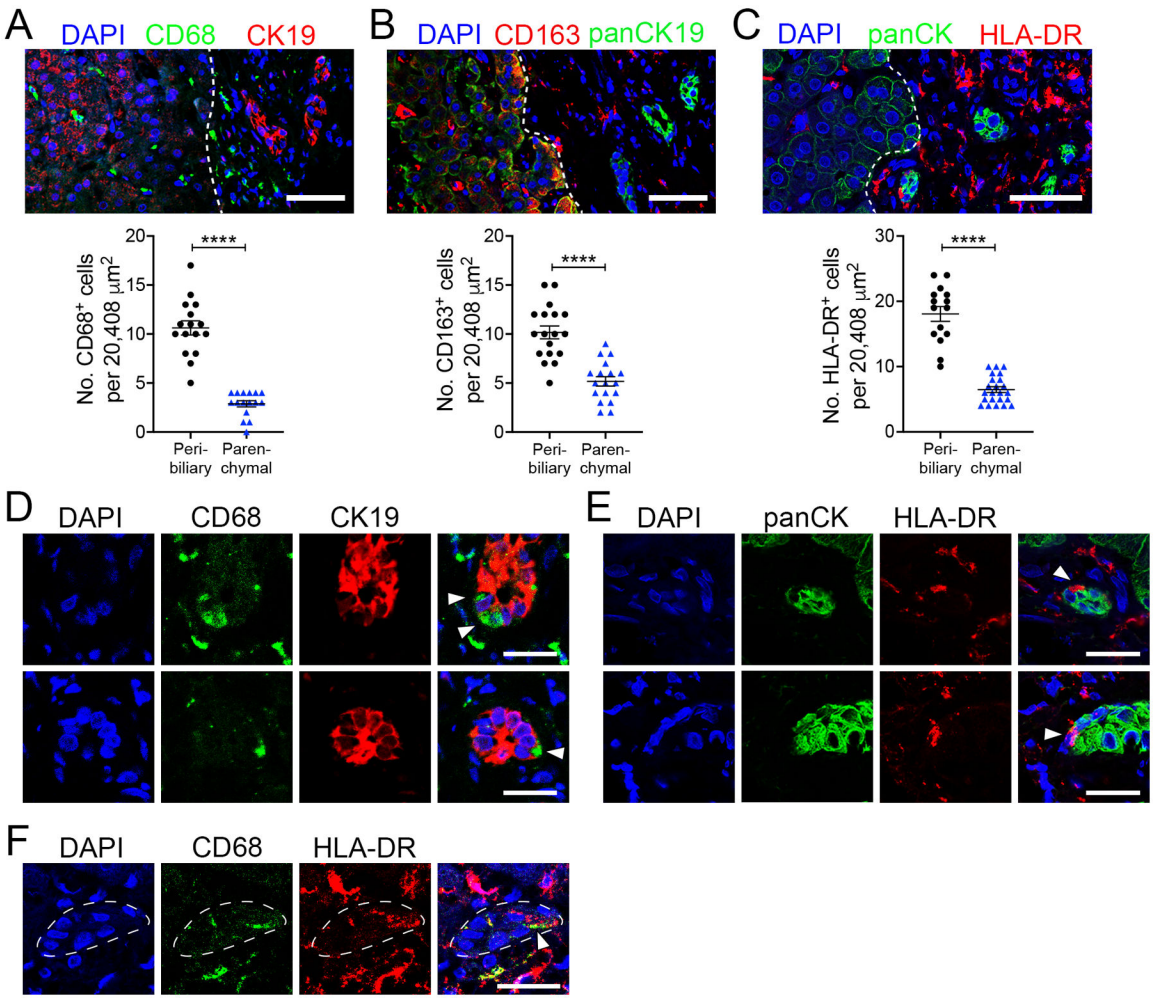

Figure 2. Increased accumulation of macrophages in the portal tract of *ANKS6* patient liver.

(**A**) CD68 (green) and CK19 (red) immunofluorescence staining in *ANKS6* patient liver biopsy. Dashed white line demarcates the border between portal fibrosis and the liver parenchyme. Quantification of the number of $CD68^+$ cells in the peribiliary region vs the liver parenchyma per defined field, ****p<0.0001. Scale bar 50 µm.

(**B**) CD163 (red) and panCK19 (green) immunofluorescence staining in *ANKS6* patient liver biopsy. Dashed white line demarcates the border between portal fibrosis and the liver parenchyma. Quantification of the number of $CD163^+$ cells in the peribiliary region vs the liver parenchyma per defined field, ****p<0.0001. Scale bar 50 µm.

(**C**) HLA-DR (red) and panCK (green) immunofluorescence staining in *ANKS6* patient liver biopsy. Dashed white line demarcates the border between portal fibrosis and the liver parenchyma. Quantification of the number of $HLA\text{-}DR^+$ cells in the peribiliary region vs the liver parenchyma per defined field, ****p<0.0001. Scale bar 50 µm.

(**D**) Immunofluorescence analysis reveals that $CD68^+$ macrophages (green) infiltrate (white arrows) the bile duct epithelium (red) in *ANKS6* patient liver biopsy sample. Scale bar 20 µm.

(**E**) Immunofluorescence analysis reveals that inflammatory HLA-DR$^+$ M1 macrophages (red) infiltrate (white arrows) the bile duct epithelium (green) in *ANKS6* patient liver biopsy sample. Scale bar 20 μm.
(**F**) Co-staining of CD68 and HLA-DR in bile duct infiltrating inflammatory M1 macrophages (white arrow). White dashed line demarcates bile duct. Scale bar 25 μm. Results analyzed by t-test on biological replicates with p values as indicated.

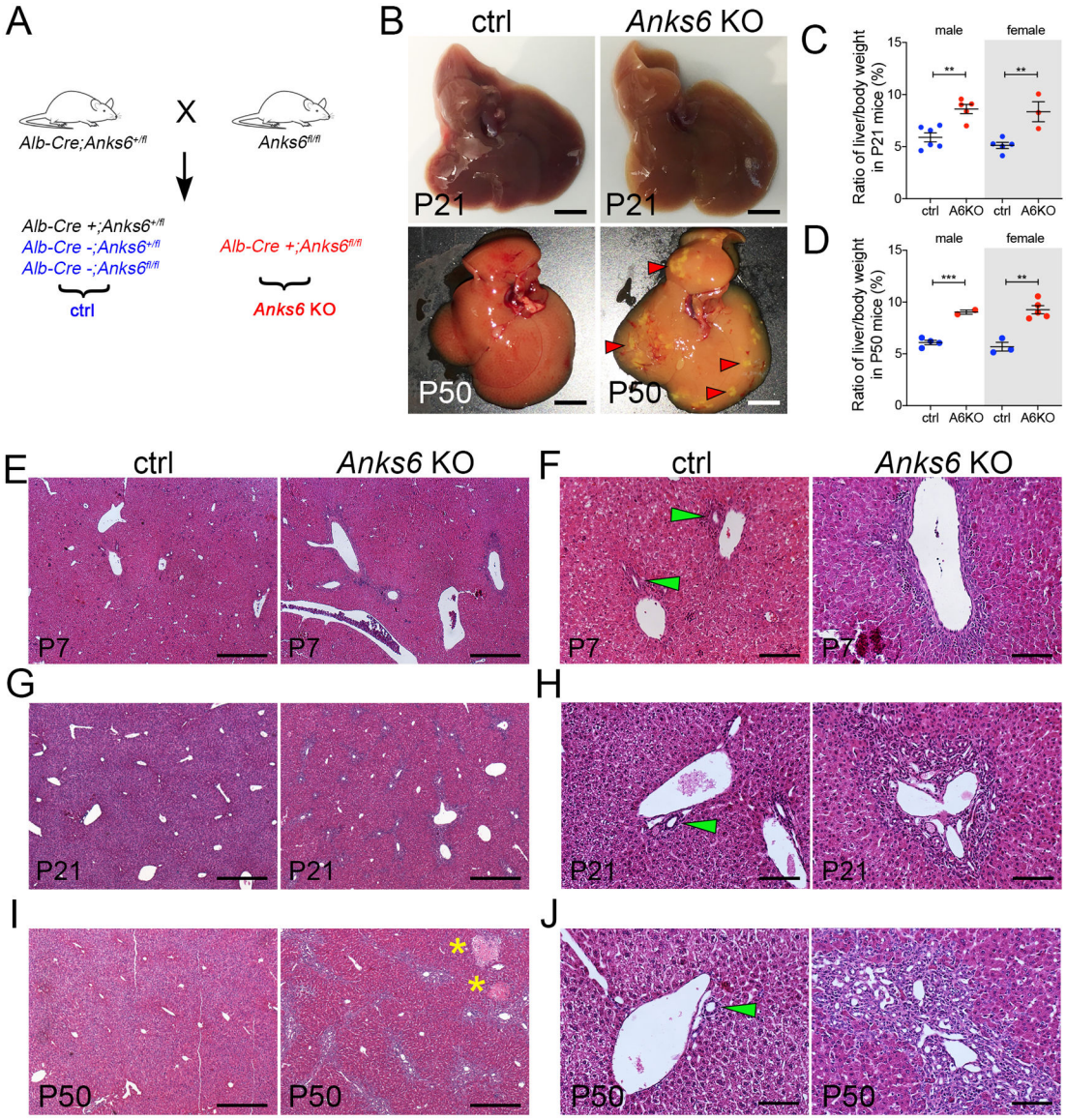

Figure 3. Liver-specific *Anks6* inactivation leads to portal malformations in mice.

(A) Schematics of the generation of liver-specific *Anks6* knockout (*Anks6* KO) mice, by crossing *AlbCre;Anks6*$^{+/fl}$ mice with *Anks6*$^{fl/fl}$ mice. *Albumin-Cre* negative littermates are used as control mice in this study.

(B) Gross morphology of control and *Anks6* KO livers at P21 and P50. Control livers have a normal morphology while *Anks6* KO livers appear paler and develop cholestasis (red arrowheads) by P50. Scale bars, 5 mm

(C,**D)** Quantification of liver to body weight ratio in *Anks6* KO and control mice at P21 (**C**) and P50 (**D**). Both, male and female *Anks6* KO mice have increased liver to body weight ratio compared to age-matched control mice, indicating that the liver phenotype is not gender-specific. n=2–5 per group. **p<0.01, ***p<0.001.

(E,**F**,**G**,**H**,**I**,**J)** Hematoxylin and eosin staining of P7 (**E**,**F**), P21 (**G**,**H**) and P50 (**I**,**J**) control and *Anks6* KO livers. Control livers show normal liver histology. In contrast, the portal areas

in *Anks6* KO livers demonstrate progressive bile duct expansion and portal fibrosis. Green arrow heads indicate bile ducts in control livers (**H**,**J**). Necrotic lobular spots (yellow stars) caused by cholestasis are visible at macroscopic view in *Anks6* KO liver at P50 (**I**). Scale bars, (**E**,**G**,**I**) 500 μm, (**F**,**H**,**J**) 100 μm.

Results analyzed by t-test on biological replicates with p values as indicated.

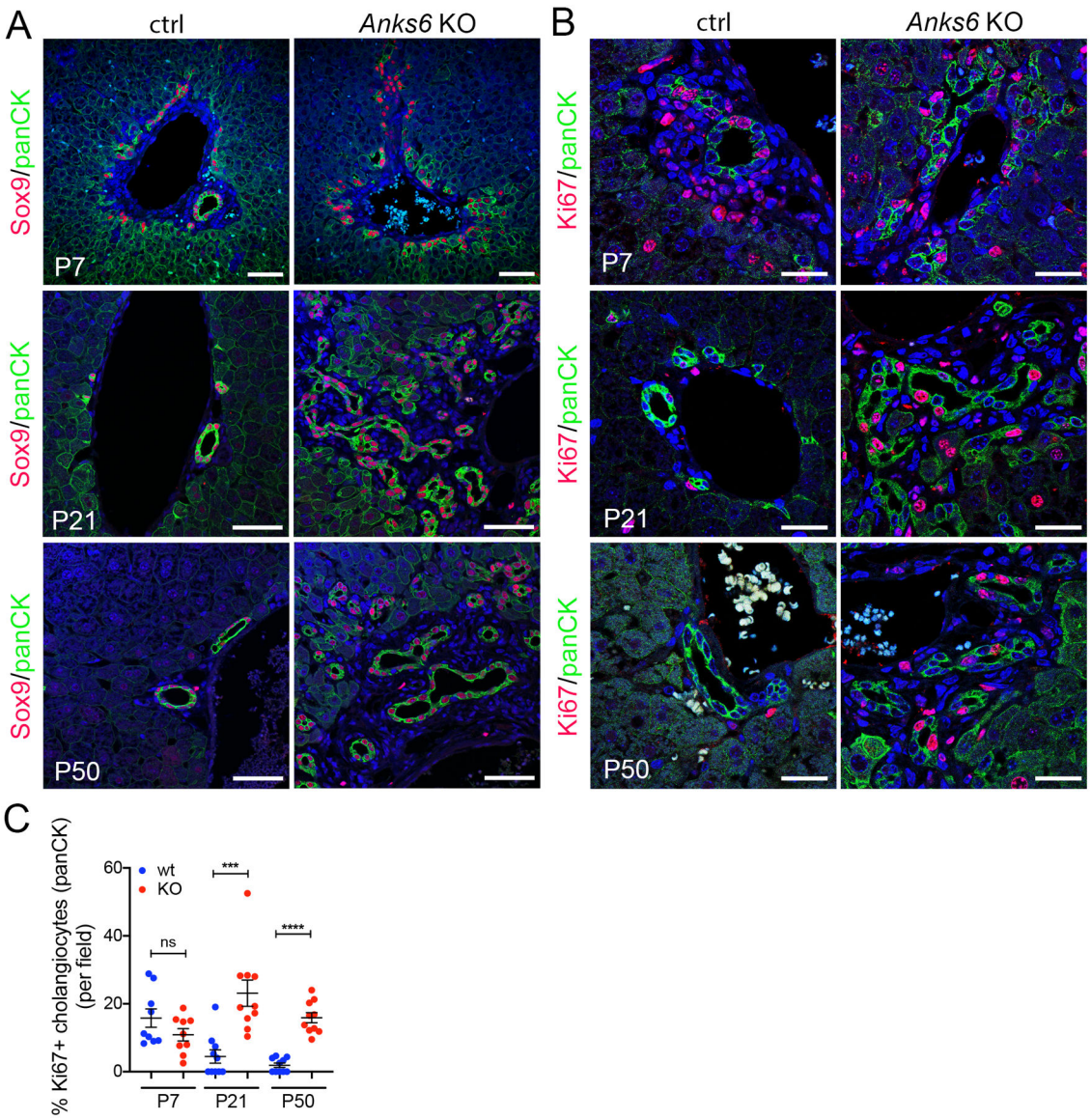

Figure 4. Increased cell proliferation underlies biliary expansion in *Anks6* KO mice.

(**A**) Immunofluorescent co-staining with Sox9 (red) and panCK (green) antibodies to compare the postnatal bile duct morphology in normal (control) vs *Anks6* KO livers at P7, P21 and P50. Scale bars 50 μm.

(**B**) Representative images of liver sections from P7, P21 and P50 postnatal stages stained with antibodies against the cell proliferation marker Ki67 (red) and panCK (green). Scale bars 25 μm.

(**C**) Quantification of Ki67-positive cholangiocytes (panCK+) in control and *Anks6* KO livers. The ratio of Ki67+ cells to panCK+ cells decreased in wild type livers with increasing age, whereas the ratio remained virtually unchanged in *Anks6* KO livers from P7 to P50. P7 (ctrl vs. *Anks6* KO; 15.78 vs.10.87, ns p=0.15), P21 (ctrl vs. *Anks6* KO; 4.481 vs. 23.12, *** p<0.001), P50 (ctrl vs. *Anks6* KO; 1.89 vs. 15.90, **** p<0.0001).

Results analyzed by t-test on biological replicates with p values as indicated.

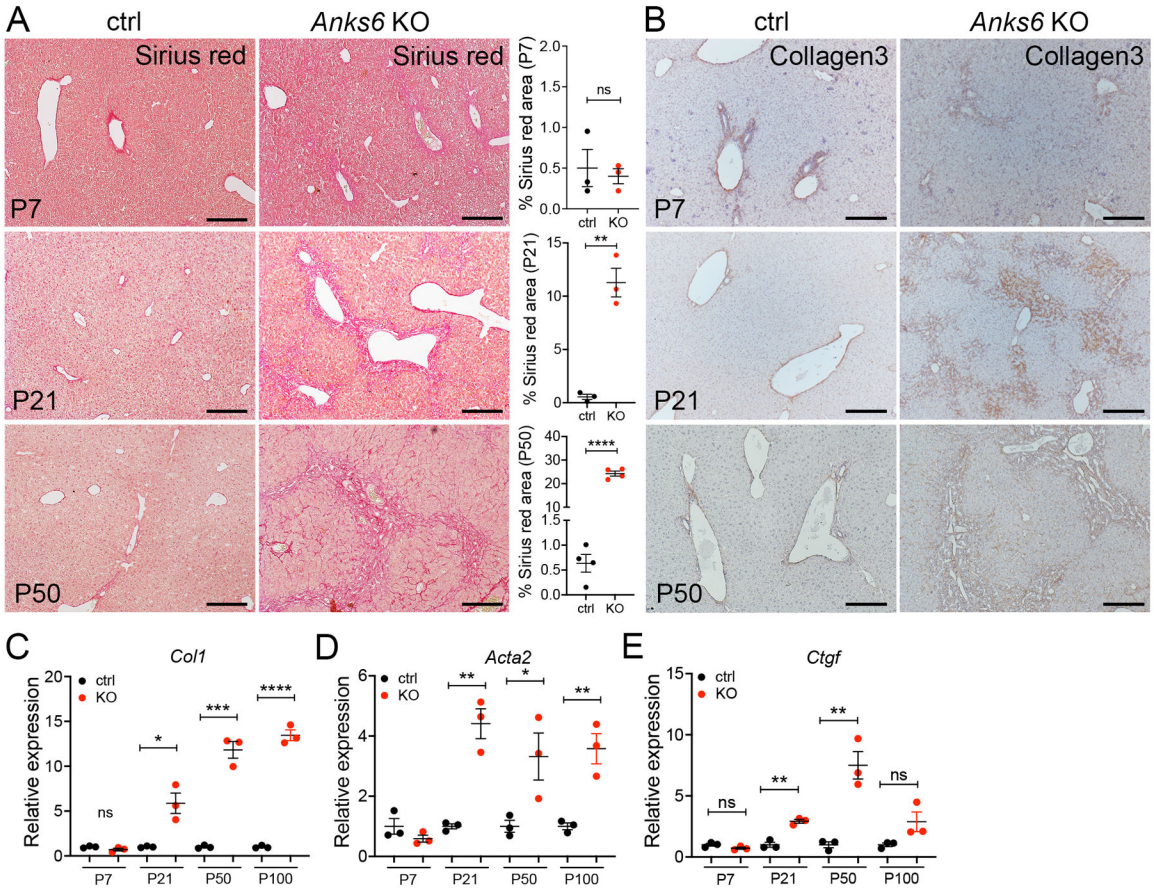

Figure 5. Rapid development of liver fibrosis in *Anks6* KO mice.

(**A**) Liver sections from control and *Anks6* KO mice at P7, P21 and P50 were stained with Sirius red to mark fibrosis. Control livers show normal levels of Sirius red staining in the portal tract denoting lack of fibrosis. Sirius red staining is normal in *Anks6* KO livers at P7, but is significantly increased in the mutant livers at P21 and P50. Note the presence of porto-portal fibrotic bridging in the livers of older *Anks6* KO mice. Quantification of Sirius red staining in P7, P21 and P50 in control and *Anks6* KO livers confirm progressive increase in Sirius red positive area in *Anks6* KO livers. n=3–4 per group, **p<0.01, ****p<0.0001. Scale bars, 200 μm.

(**B**) Immunohistochemical analysis of collagen type 3 expression in control and *Anks6* KO livers at P7, P21, and P50. Scale bars, 200 μm.

(**C-E**) Gene expression analysis of *Col1* (C), *Acta2* (D) and *Ctgf* (E) in P7, P21, P50 and P100 livers. n=3 per group, *p<0.05, **p<0.01, ***p<0.001, ****p<0.0001. Results analyzed by t-test on biological replicates with p values as indicated.

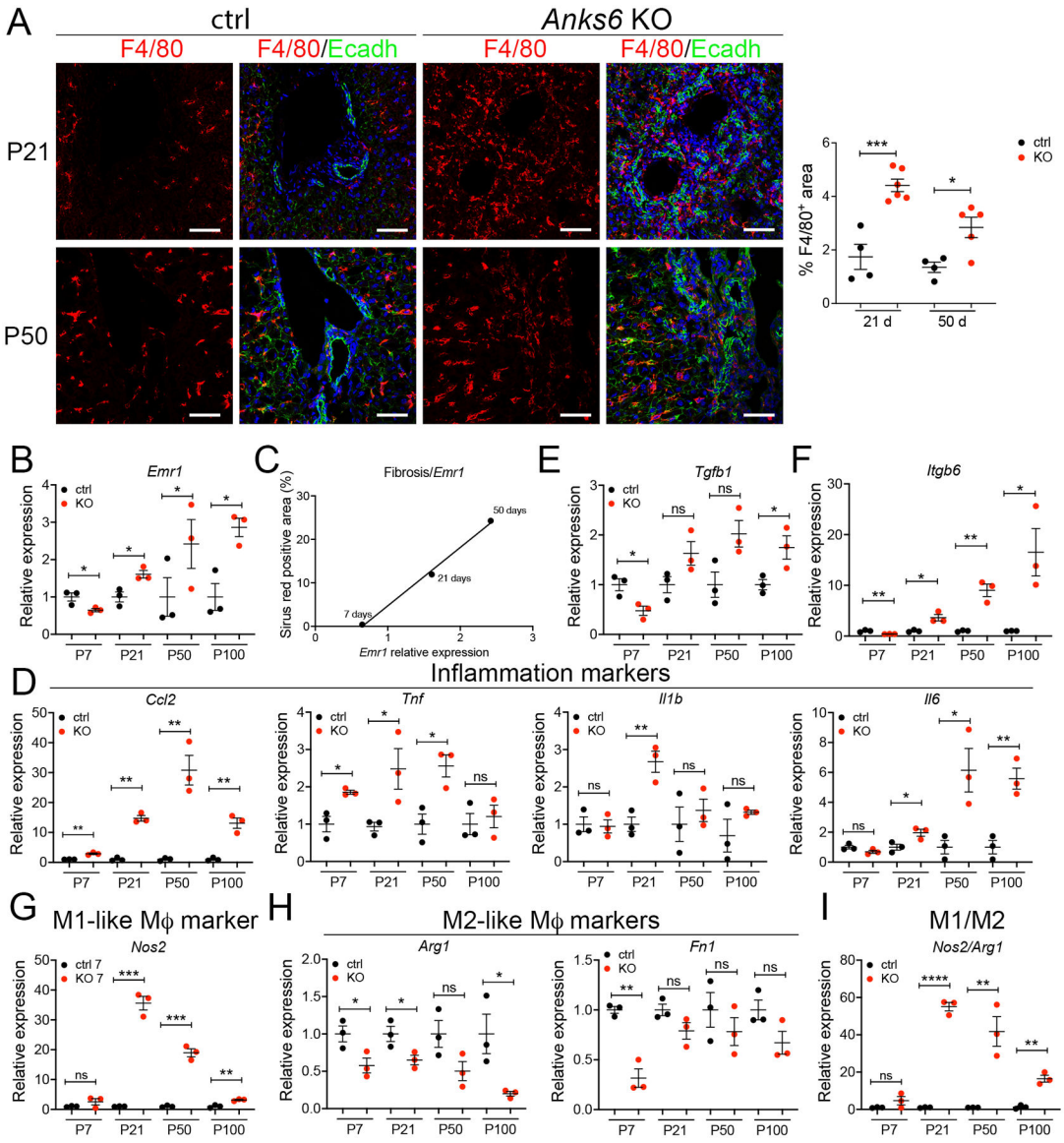

Figure 6. Portal fibrosis is associated with macrophage recruitment in *Anks6* KO livers.

(**A**) Immunofluorescent analysis of macrophage (F4/80, red) recruitment to the peribiliary (Ecadherin, green) region in P21 and P50 control and *Anks6* KO livers. Scale bars 50 μm. Quantification of F4/80^{+} macrophages in control and *Anks6* KO livers. n=4–5 per group *p<0.05, **p<0.001.

(**B**) qPCR analysis of *Emr1* expression in control and *Anks6* KO livers at P7, P21, P50 and P100. n=3 per group, *p<0.05.

(**C**) The extent of portal fibrosis (Sirius red) strongly and positively correlates with *Emr1*(F4/80) expression in *Anks6* KO livers (r = 0.93, *p<0.05).

(**D**) qPCR analysis of pro-inflammatory cytokine (*Ccl2*, *Tnfa*, *Il1b*) and anti-inflammatory cytokine *Il6* gene expression in control and *Anks6* KO livers at P7, P21, P50 and P100. n=3 per group, *p<0.05, **p<0.01.

(**E**) qPCR analysis of *Tgfb1* gene expression in control and *Anks6* KO livers at P7, P21, P50 and P100. n=3 per group, *p<0.05.
(**F**) qPCR analysis of *Itgb6* gene expression in control and *Anks6* KO livers at P7, P21, P50 and P100. n=3 per group, *p<0.05, **p<0.01.
(**G**) qPCR analysis of M1-like macrophage polarization marker *Nos2* in control and *Anks6* KO livers at P7, P21, P50 and P100. n=3 per group, **p<0.01, ***p<0.001.
(**H**) qPCR analysis of M2-like macrophage polarization markers *Arg1* and *Fn1* in control and *Anks6* KO livers at P7, P21, P50 and P100. n=3 per group, *p<0.05, **p<0.01.
(**I**) The gene expression ratio of *Nos2* and *Arg1* steadily declines after peaking at P21, suggesting that the immune cell composition in *Anks6* KO livers transitions from mostly inflammatory M1-like macrophages to less inflammatory and more pro-fibrotic M2-like macrophages in older *Anks6* KO livers. n=3 per group, **p<0.01, ****p<0.0001.
Results analyzed by t-test on biological replicates with p values as indicated.

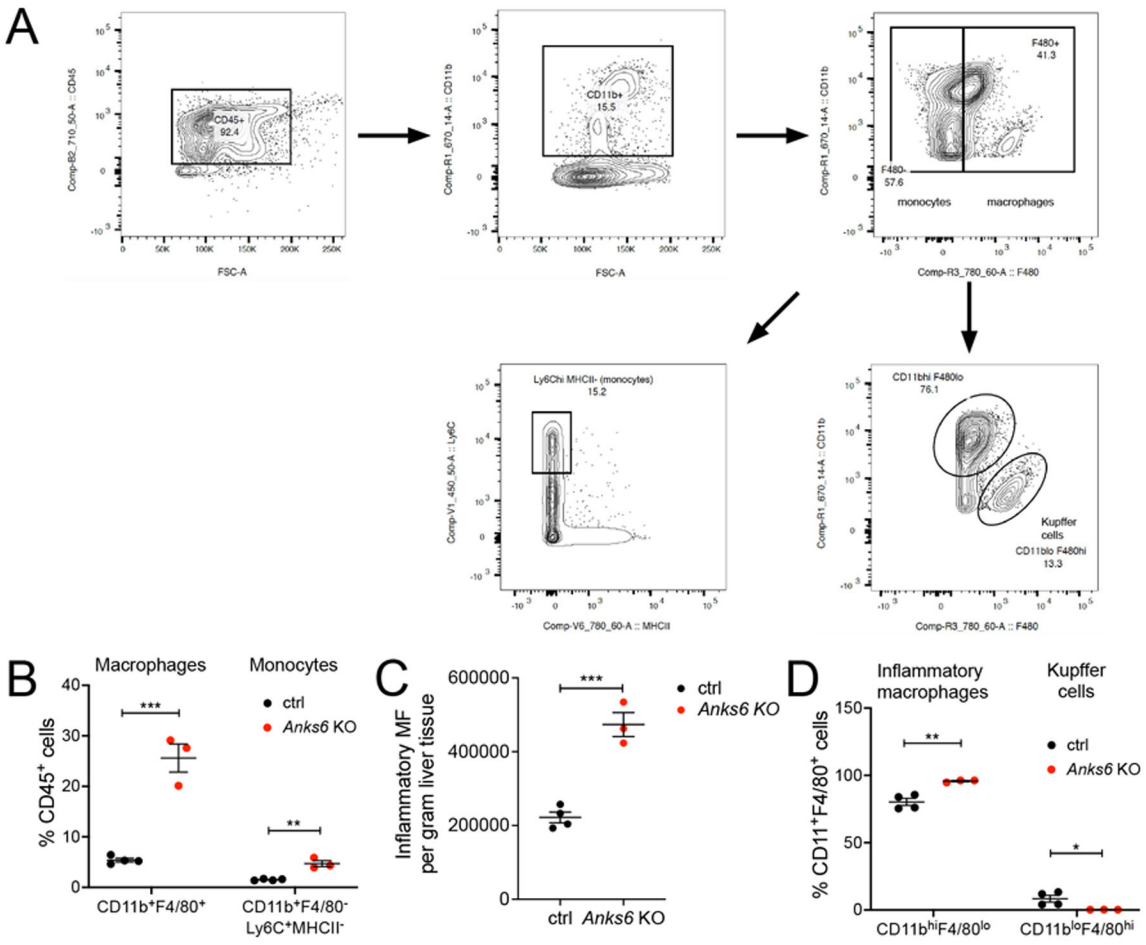

Figure 7. Flow cytometry analysis and phenotyping of monocyte/macrophage cell populations in control and *Anks6* KO livers.

(**A**) Flow cytometry gating strategies and gating controls for phenotyping liver monocytes/macrophages.

(**B**) Whole livers from 28 days old control and *Anks6* KO mice (n=3–4) were processed to single cell suspensions and absolute numbers of infiltrating monocytes ($CD11b^+F4/80^-Ly6C^+MHCII^-$) and macrophages ($CD11b^+F4/80^+$) were determined by flow cytometry. Cell numbers were normalized to average liver weight, as shown in Supplementary Figure 3D. ***p<0.001.

(**C**) Quantification of the absolute numbers of $CD11b^{hi}F4/80^{lo}$ inflammatory macrophages in *Anks6* KO livers.

(**D**) Percent of inflammatory macrophages ($CD11b^{hi}F4/80^{lo}$) and Kupffer ($CD11b^{lo}F4/80^{hi}$) cells in control vs. *Anks6* KO livers. *p<0.05, **p<0.01; n=3–4.

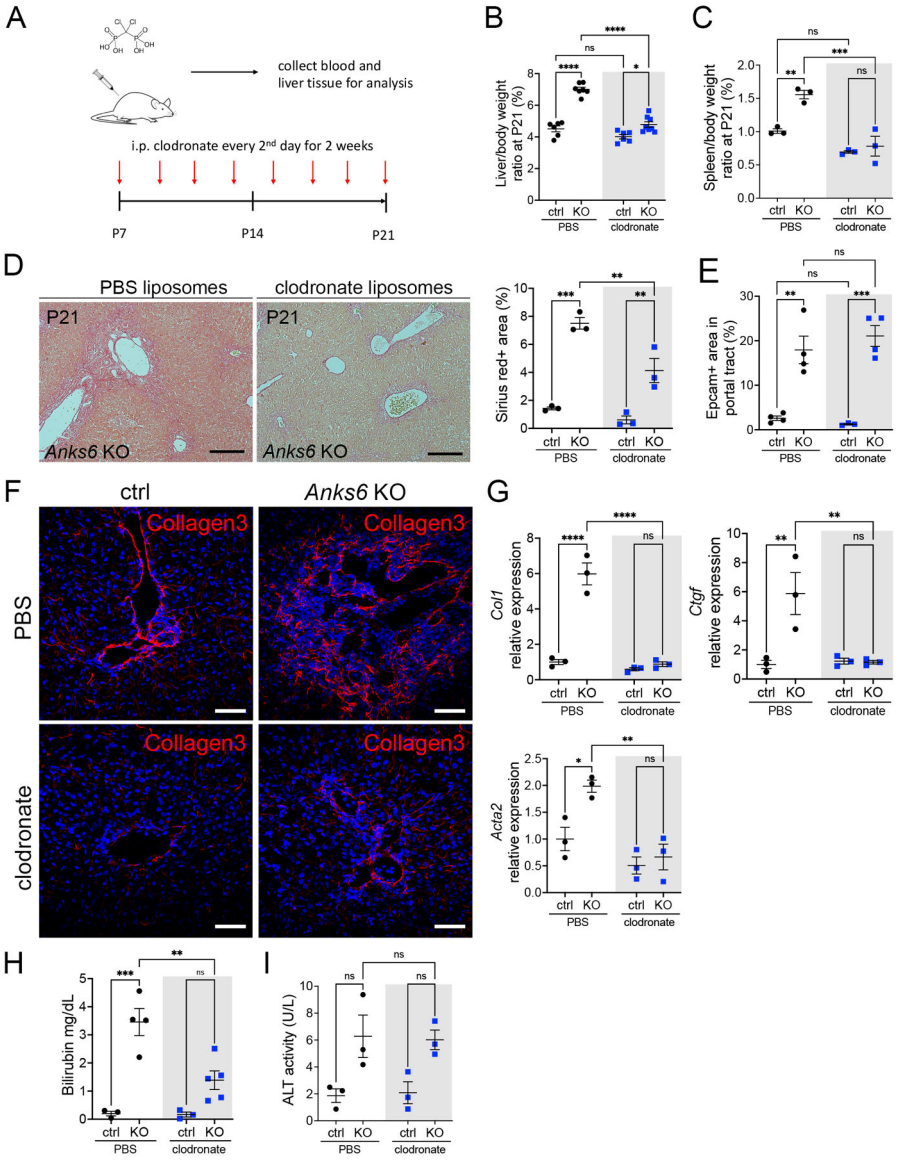

Figure 8. Clodronate treatment improves *Anks6* KO liver histology and function.

(**A**) Schematic overview of the clodronate liposome and PBS liposome treatment protocol in mice. Liposomes were administered via intraperitoneal injection at 100 mg/kg on every second day.

(**B**) Quantification of liver to body weight ratio in chlodronate vs PBS liposome treated *Anks6* KO and control mice. Male and female mice are grouped together, since liver/body weight ratio is not gender-specific (see Figure 2C,D). n=3–5 per group. ***p<0.001.

(**C**) Quantification of spleen to body weight ratio in chlodronate vs PBS liposome treated *Anks6* KO and control mice. Male and female mice are grouped together. n=3 per group. ***p<0.001.

(**D**) Liver sections from P21 *Anks6* KO mice treated with PBS liposome or clodronate liposome stained for Sirius red to mark fibrosis. Clodronate treatment leads to a significant

reduction in Sirius red-positive area in *Anks6* KO livers as shown by quantification. n=3–4 each, **p<0.01, ****p<0.0001. Scale bars 200 μm.

(**E**) Clodronate treatment does not lead to a reduction in $Epcam^{+}$ bile duct area in Anks6 KO livers. n=3–4 each, **p<0.01, ***p<0.001.

(**F**) Immunofluorescence staining of collagen type 3 expression in chlodronate vs PBS liposome treated control and *Anks6* KO livers at P21. Scale bars, 50 μm.

(**G**) Gene expression analysis of *collagen 1*, *Acta2* and *Ctgf* in chlodronate vs PBS liposome control and *Anks6* KO livers. n=3 each, *p<0.05, **p<0.01.

(**H**) Chlodronate liposome treatment significantly reduces total bilirubin levels in *Anks6* KO mice. Male and female mice are grouped together. n=3–5 each. *p<0.05, **p<0.01.

(**I**) ALT levels are slightly but not significantly increased in *Anks6* KO mice at P21 and P50. Clodronate treatment from P7 to P21 does not affect the levels of ALT in control or *Anks6* KO mice. n=3 each.

Results analyzed by 2-way ANOVA on biological replicates with p values as indicated.

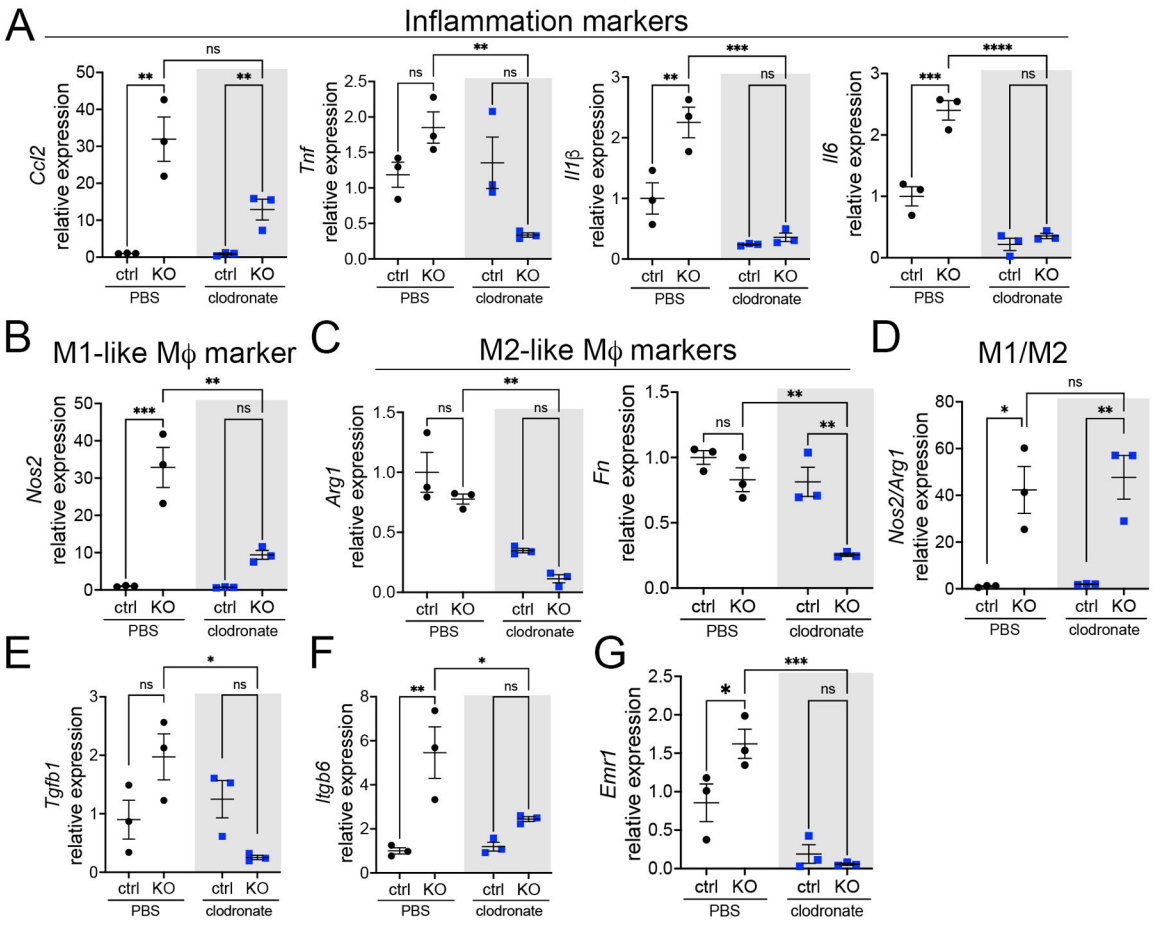

Figure 9. Clodronate liposomes reduce inflammatory signaling in *Anks6* KO livers but do not alter M1/M2-specific gene expression ratio

(**A**) qPCR analysis of pro-inflammatory cytokines (*Ccl2*, *Tnfa*, *Il1b*) and the anti-inflammatory cytokine *Il6* gene expression in P21 control and *Anks6* KO livers treated with PBS or clodronate liposomes. n=3 each, *p<0.05, **p<0.01, ***p<0.001.

(**B**) qPCR analysis of M1-like macrophage polarization marker *Nos2* in P21 control and *Anks6* KO livers treated with PBS or clodronate liposomes. n=3 each, *p<0.05, **p<0.01.

(**C**) qPCR analysis of M2-like macrophage polarization markers *Arg1* and *Fn1* in P21 control and *Anks6* KO livers treated with PBS or clodronate liposomes. n=3 each, **p<0.01, ***p<0.001.

(**D**) The gene expression ratio of *Nos2* and *Arg1* is not altered in P21 PBS liposome vs. clodronate liposomes treated *Ansk6* KO livers. n=3 each, *p<0.05, **p<0.01.

(**E**) *Tgfb1* gene expression is significantly downregulated in P21 *Anks6* KO livers after clodronate treatment. n=3 per group, *p<0.05.

(**F**) *Itgb6* gene expression is significantly downregulated in P21 *Anks6* KO livers after clodronate treatment. n=3 per group, *p<0.05.

(**G**) *Emr1* gene expression is significantly downregulated in P21 *Anks6* KO livers after clodronate treatment. n=3 per group, *p<0.05, **p<0.01.

Results analyzed by 2-way ANOVA on biological replicates with p values as indicated.